Cosmic pears from the Havelland (Germany): Ribbeck, the twelfth recorded aubrite fall in history

Addi Bischoff, Markus Patzek, Jean-Alix Barrat, Jasper Berndt, Henner Busemann, Detlev Degering, Tommaso Di Rocco, Mattias Ek, Dennis Harries, Jose Godinho, et al.

Cosmic pears from the Havelland (Germany): Ribbeck, the twelfth recorded aubrite fall in history

Addi BISCHOFF [1]*, Markus PATZEK [1], Jean-Alix BARRAT[2,3], Jasper BERNDT[4],
Henner BUSEMANN [5], Detlev DEGERING[6], Tommaso DI ROCCO[7], Mattias EK[5],
Dennis HARRIES[8], Jose R. A. GODINHO[9], Dieter HEINLEIN[10], Armin KRIELE[11],
Daniela KRIETSCH [5], Colin MADEN [5], Oscar MARCHHART [12], Rachael M. MARSHAL[1],
Martin MARTSCHINI [12], Silke MERCHEL [12], Andreas MÖLLER[13], Andreas PACK[7],
Herbert RAAB[14], Maximilian P. REITZE [1], Ina RENDTEL[15], Miriam RÜFENACHT[5],
Oliver SACHS[16], Maria SCHÖNBÄCHLER [5], Anja SCHUPPISSER[5], Iris WEBER [1],
Alexander WIESER [12], and Karl WIMMER[17]

[1]Institut für Planetologie, University of Münster, Münster, Germany
[2]Univ Brest, CNRS, Ifremer, IRD, LEMAR, Institut Universitaire Européen de la Mer (IUEM), Plouzané, France
[3]Institut Universitaire de France, Paris, France
[4]Institut für Mineralogie, University of Münster, Münster, Germany
[5]Institute of Geochemistry and Petrology, Zurich, Switzerland
[6]VKTA—Strahlenschutz, Analytik & Entsorgung Rossendorf e. V., Dresden, Germany
[7]Geowissenschaftliches Zentrum, Universität Göttingen, Göttingen, Germany
[8]European Space Resources Innovation Centre (ESRIC), Luxembourg Institute of Science and Technology (LIST), Belvaux, Luxembourg
[9]Helmholtz-Zentrum Dresden-Rossendorf, Helmholtz Institute Freiberg for Resource Technology, Freiberg, Germany
[10]German Fireball Network, Augsburg, Germany
[11]German Engineering Materials Science Centre (GEMS), Heinz Maier-Leibnitz Zentrum (MLZ), Helmholtz-Zentrum Hereon, Garching, Germany
[12]Faculty of Physics, Isotope Physics, University of Vienna, Vienna, Austria
[13]Arbeitskreis Meteore (AKM) e.V., Berlin, Germany
[14]Johannes-Kepler-Sternwarte Linz, Linz, Austria
[15]Arbeitskreis Meteore (AKM) e.V., Potsdam, Germany
[16]Freunde RiesKraterMuseum e.V., Nördlingen, Germany
[17]Salvatorgasse 12, Nördlingen, Germany

*Correspondence
Addi Bischoff, Institut für Planetologie, University of Münster, Wilhelm-Klemm-Str. 10, Münster D-48149, Germany.
Email: bischoa@uni-muenster.de

Abstract–In 1889 the German poet and novelist Theodor Fontane wrote the popular literary ballad "Herr von Ribbeck auf Ribbeck im Havelland." The Squire von Ribbeck is described as a gentle and generous person, who often gives away pears from his pear trees to children passing by and continued donating pears after his death. Now, 135 years later the rock called *Ribbeck* is giving us insight into processes that happened 4.5 billion years ago. The meteorite Ribbeck (official find location: 52°37′15″N, 12°45′40″E) fell January 21, 2024, and has been classified as a brecciated aubrite. This meteoroid actually entered the Earth's atmosphere at 00:32:38 UTC over Brandenburg, west of Berlin, and the corresponding fireball was recorded by professional all sky and video cameras. More than 200 pieces (two proved by radionuclide analysis to belong to this fresh fall) were recovered totaling about 1.8 kg. Long-lived radionuclide and noble gas data are consistent with long cosmic ray exposure (55–62 Ma) and a preatmospheric radius of

Ribbeck between 20 and 30 cm. The heavily brecciated aubrite consists of major (76 ± 3 vol%) coarse-grained FeO-free enstatite ($En_{99.1}Fs_{<0.04}Wo_{0.9}$), with a significant abundance (15.0 ± 2.5 vol%) of albitic plagioclase ($Ab_{95.3}An_{2.0}Or_{2.7}$), minor forsterite ($5.5 \pm 1.5$ vol%; $Fo_{99.9}$) and 3.5 ± 1.0 vol% of opaque phases (mainly sulfides and metals) with traces of nearly FeO-free diopside ($En_{53.2}Wo_{46.8}$) and K-feldspar ($Ab_{4.6}Or_{95.4}$). The rock has a shock degree of S3 (U-S3), and terrestrial weathering has affected metals and sulfides, resulting in the brownish appearance of rock pieces and the partial destruction of certain sulfides already within days after the fall. The bulk chemical data confirm the feldspar-bearing aubritic composition. Ribbeck is closely related to the aubrite Bishopville. Ribbeck does not contain solar wind implanted gases and is a fragmental breccia. Concerning the Ti- and O-isotope compositions, the data are similar to those of other aubrites. They are also similar to E chondrites and fall close to the data point for the bulk silicate Earth (BSE). Before the Ribbeck meteoroid entered Earth's atmosphere, it was observed in space as asteroid 2024 BX1. The aphelion distance of 2024 BX1's orbit lies in the innermost region of the asteroid belt, which is populated by the Hungaria family of minor planets characterized by their E/X-type taxonomy and considered as the likely source of aubrites. The spectral comparison of an average large-scale emission spectrum of Mercury converted into reflectance and of the Ribbeck meteorite spectrum does not show any meaningful similarities.

INTRODUCTION

Recently, astronomer Krisztián Sárneczky discovered three small asteroids (2022 EB5, 2023 CX1 and 2024 BX1) from the Piszkéstet Station of the Konkoly Observatory in Hungary's Mátra Mountains before they entered the Earth's atmosphere. On January 20, 2024, at 21:48 UTC, Sárneczky detected the asteroid 2024 BX1, also known as Sar2736, which was identified by NASA and ESA impact hazard assessment systems as a potential impactor and meteorite dropper. The calculated impact time was determined to be 0:33 UTC on January 21 (Spurný et al., 2024). This was the eighth asteroid that has been discovered shortly before entering the Earth's atmosphere.

This meteoroid actually entered the Earth's atmosphere on January 21, 2024, at 00:32:38 UTC over Brandenburg, near the village Nennhausen and the city of Rathenow in Havelland, west of Berlin. The corresponding fireball was recorded by professional All Sky and video cameras (European Network, AllSky7). Due to the timely advance warning and announcement, this bolide was also observed and registered by many eyewitnesses.

The analysis of the meteoroid's atmospheric trajectory and the strewn field calculations were performed by Pavel Spurný and Jiri Borovička (Astronomical Institute of the Czech Academy of Sciences). According to their analysis, a small asteroid body, estimated to be ~140 kg (Spurný et al., 2024), entered the atmosphere at a very steep angle, lost a large part of its initial mass during the about 5 s luminous flight and fragmented heavily. The wind profile models used showed that strong winds blew the remaining meteorite fragments in a southeasterly direction, so that

the meteorites fell to Earth south of the village of Ribbeck, between Retzow and Nauen. Spectral observations of the bright bolide with the European Fireball Network stations indicated that the meteorite material is poor in iron and rich in magnesium (possibly enstatite).

Starting on 22 January, searches were conducted by scientists and students from the Museum of Natural History in Berlin, the German Aerospace Center (DLR), the Berlin universities, members of the Meteor Working Group (*Arbeitskreis Meteore* [AKM]), as well as by individuals and groups of amateur or professional meteorite hunters and collectors.

The first meteorite find was reported on 25 January by Polish searchers close to the village of Ribbeck (State of Brandenburg) about 50 km west of Berlin (Germany). The achondritic rock was broken up at the impact into three fragments totaling 171 g. During the next weeks, numerous fragments ranging from 212 to <2 g were recovered in the predicted strewnfield. To date, 202 pieces with a total weight of 1784.7 g have been retrieved (Table S1). The recovered samples are not totally black as initially expected; the hand specimens typically contain large light-colored fragments and often have an unusual white vesicular fusion crust (Figure 1a–d). The rock specimens studied here in detail were recovered January 27, 2024, 6 days after the collision of the meteoroid with the Earth (Figure 2a,b).

The meteorite Ribbeck (official find location: 52°37′15″N, 12°45′40″E) has been classified as a brecciated aubrite (The Meteoritical Bulletin, 2024) and initial data were presented at the Meteoritical Society Meeting in Brussels (Bischoff & Patzek, 2024; Hamann et al., 2024; Van den Neucker et al., 2024) and by Cantillo et al. (2024)
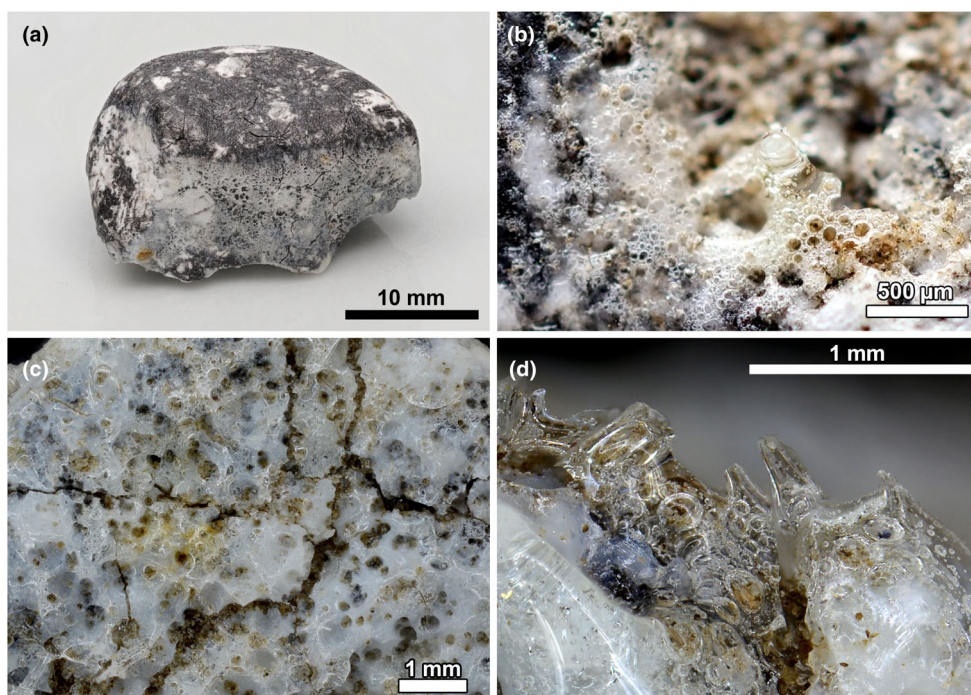
FIGURE 1. (a) Oriented, inhomogeneous fragment F07 with a light, porous fusion crust at the lower side. (b) Details of a vesicular, white fusion crust on fragment F02; Photo: D. Göttlich. (c) Foamy vesicular structure of the fusion crust on sample F82 with clearly visible cracks; Photo: O. Lenzen. (d) Outside structure of the clear, glassy fusion crust of F82; Photo: O. Lenzen.

and Rendtel et al. (2024). Aubrites are rare types of meteorites and are named after an 800 g meteorite that fell on September 14, 1836, at a place called Aubres, east of Nyons, France (The Meteoritical Bulletin, 2024). Until the fall of Ribbeck, only 11 other aubrite falls had been recorded, while 76 finds (including six anomalous aubrites) are listed in the meteorite database. The largest aubrite is Norton County with a mass of ~1.1 t, located in the Geological Museum of the University of New Mexico in Albuquerque. Keil (2010) published an excellent summary on many aspects concerning research on this type of meteorite sample (see also, e.g., Fogel, 1997; Keil et al., 1989; Lipschutz et al., 1988; Lorenz et al., 2005; Love et al., 2005; McCoy et al., 1999; Okada et al., 1988; Watters & Prinz, 1979; Watters & Prinz, 1980; Wilbur et al., 2022).

Keil (2010) highlighted that aubrites are a fascinating group of meteorites because they are rocks of extremes. According to some of their main properties, he indicated that these rocks may represent endmembers in the spectrum of formation conditions for igneous meteorites from asteroids. As an important example, he considered that aubrites might form under highly reducing conditions (e.g., Keil, 1989, 2010; Krot et al., 2004; Mittlefehldt, 2004; Mittlefehldt et al., 1998; Okada et al., 1988; Wilbur et al., 2022), resulting in the observation that normally lithophile elements such as Ti, Cr, Mn, Na

and others partly behave as chalcophile elements (i.e., occur in sulfides) or partly as siderophile elements (i.e., Si occurs in metallic Fe,Ni). These reducing formation conditions also lead to the formation of almost FeO-free silicates like enstatite, the predominant mineral phase in aubrites. Enstatite is typically in paragenesis with variable amounts of albitic plagioclase, nearly FeO-free diopside and forsterite (e.g., Watters & Prinz, 1979), Si-bearing metallic Fe,Ni (e.g., Casanova et al., 1993) and Ti-Cr-bearing troilite (e.g., Keil, 2010; Keil & Fredriksson, 1963). Keil (2010) also listed many rare and minor minerals, many of which form only under highly reducing conditions and are unknown from Earth. Several of these mineral phases also occur in Ribbeck and will be considered and described below in detail.

The village of Ribbeck is well known in German-speaking areas thanks to a poem by Theodor Fontane "Herr von Ribbeck zu Ribbeck im Havelland" (English: "Squire von Ribbeck at Ribbeck in Havelland"), providing some insight into German culture (https://www.vonribbeck.de/ribbeck-international/; see poem and a link to the song by Achim Reichel in the Supporting information). The story basically deals with a pear tree, the cycle of life, and charitable contributions to society. The Squire von Ribbeck, who donated pears to children throughout his life, asks before his death to put pears into

FIGURE 2. The studied fragments from AKM01 (compare Table S1): (a) The 4.3 g sample of Ribbeck found January 27, 2024, in a winter rapeseed field next to a plant leaf. (b) The ~20 g piece used for non-destructive gamma spectrometry found nearby (Photo: P. Lindner).

his grave so that the grown pear trees would continue to provide free pears to children even after he is gone.

SAMPLES AND METHODS—SUMMARY

Different analytical methods were applied to obtain information about the meteorite class of the Ribbeck samples used in this study and to reveal details on chemical, physical, isotopic and mineralogical features and characteristics of the rock. Here, we briefly present the studied samples and summarize the analytical procedures. Further details are given in the Supporting information.

Samples

A 4.3 g Ribbeck specimen resulting from the shattered fragment AKM01 (Supporting information; Table S1) was taken to prepare polished sections, fragments and homogeneous powder for the various research methods. This sample used for mineralogical, isotopic and chemical studies was found in the northern part of a winter rapeseed field next to a plant leaf (Figure 2a). It looked like a whitish-gray inhomogeneous rock (compare Figure S1). While other small (local) rocks were partly embedded into the soil, the meteorite specimen was exposed on the surface. It was easy to spot because no other stones were visible in the vicinity. It was one of several pieces found in an area of about 4 m². Optically very similar samples (Figure S1; Table S1) were used for gamma spectrometry (another fragment of about 20 g from AKM01 and fragment AKM05) and for determining the density (F05, F06, F07).

Methods Summary

Several thin (PL24001, PL24008) and thick sections (PL24002) from the 4.3 g piece of the shattered fragment AKM01 were studied using optical and electron microscopy (SEM) at the Institut für Planetologie (University of Münster). Most chemical data were obtained by electron microprobe analysis (EPMA) at the Institut für Mineralogie (Münster). The same instrument was used to determine the modal composition corrected after the procedure of Van der Plas and Tobi (1965).

After preparation of a homogenous powder of ~0.75 g from 4.3 g piece AKM01, a 155 mg whole-rock sample was analyzed for major and trace element concentrations by inductively coupled plasma atomic emission spectroscopy (ICP-AES) and inductively coupled plasma sector field mass spectrometry (ICP-SFMS) at the University of Brest following the procedure described by Barrat et al. (2012) and Barrat, Gillet, et al. (2016). Cosmogenic as well as primordial radionuclide concentrations were analyzed on two specimens of 19.55 g (from AKM01; Table S1) and 25.5 g (AKM05; Table S1) by non-destructive gamma spectrometry in the underground laboratory Felsenkeller (Niese et al., 1998) of the VKTA Rossendorf (Dresden).

The bulk oxygen isotope composition was analyzed by means of laser fluorination in combination with gas source mass spectrometry (University of Göttingen). More information is presented in the Supporting information and given in Pack and Herwartz (2014), Herwartz et al. (2014), Pack et al. (2016, 2017) and Peters et al. (2020).

For the Ti isotope analyses, powdered sample of Ribbeck (together 48.9 mg) were dissolved and purified using ion exchange chromatographic procedures. Titanium isotope analyses were carried out using a Thermo Fisher Scientific Neptune Plus multicollector inductively coupled plasma mass spectrometer (MC-ICPMS) at the Institute of Geochemistry and Petrology at ETH Zurich. The analytical procedures followed those described in Bischoff, Barrat, et al. (2019), Schönbächler
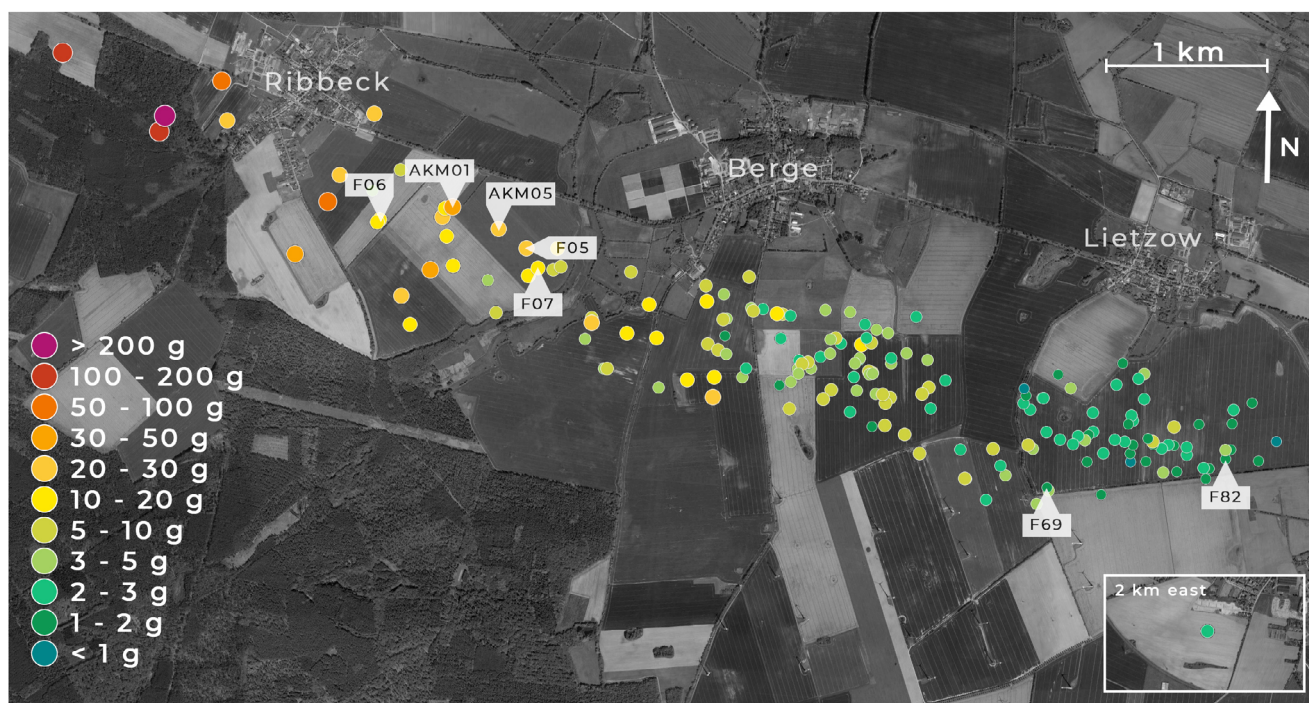
FIGURE 3. The strewnfield with the Ribbeck samples registered by our team. Source of base map: Google Earth. The studied samples are marked by arrows.

et al. (2004), Williams et al. (2021) and Rüfenacht et al. (2023) and are described in more detail in the Supporting information.

Both methods analyzing cosmogenic nuclides used powdered aliqouts of the 0.75 g from AKM01. The noble gases He-Xe present in the bulk sample of 13.822 mg were analyzed at ETH Zurich using the standard procedures described in detail by Riebe et al. (2017). Accelerator mass spectrometry (AMS) is the method of choice for detecting long-lived cosmogenic radionuclides such as ^{26}Al and ^{41}Ca using the worldwide unique development at the Vienna Environmental Research Accelerator (VERA) (Martschini et al., 2022).

Regarding further mineralogical and physical properties, the density was determined at the Helmholtz-Zentrum Hereon (Garching, Germany), at the Luxembourg Institute of Science and Technology (Belvaux, Luxembourg), and using computed tomography at the Helmholtz-Institute Freiberg for Resource Technology. The magnetic susceptibility (MS) of the meteorite was measured with the handheld device SM-30 from ZH Instruments (www.zhinstruments.cz) in Nördlingen (Germany). Fourier transform infrared spectroscopy (FT-IR) spectroscopic measurements were undertaken at the Institut für Planetologie (University of Münster, Germany). Further Raman spectroscopy investigations were done at the Institut für Mineralogie

(University of Münster, Germany; see Supporting information).

SAMPLES AND FIND LOCATIONS OF THE RIBBECK METEORITE

In the days following the meteorite fall, 202 individual meteorite samples totaling a mass of ~1.8 kg were recovered within a strewnfield of about 1.5 km × 10 km (Figure 3). Images of typical locations of the find area are given in Figure 4. The largest samples have masses of 212 and 171 g, respectively. The latter object was broken into three pieces. The cumulative mass-number distribution of individual recovered Ribbeck meteorites and their comparison with distributions of samples of other meteorite falls are discussed below. Ribbeck samples frequently appear fragmented due to the stones' extreme friability. Many of the recovered rocks have remarkably wide visible cracks. Some typical images of the currently studied samples are given in Figure S1, and images of other recovered samples are presented in Figure S2. During the first weeks after the fall event, rocks belonging to the Ribbeck meteorite fall were easily identified due to their pungent H_2S odor resulting from the rapid destruction of sulfides (especially oldhamite [CaS; see below]).

FIGURE 4. (a) Western entry of the small village of Ribbeck, part of the city of Nauen in the Havelland. Town sign in late January 2024 at the time of farmer protests against German political decisions. (b) Typical landscape in the western part of the strewnfield, where the largest samples were found by Polish searchers. (c) Forest in the central part of the strewnfield. (d) Field of winter barley close to the village of Ribbeck. (e) Harvested field close to the forest southwest of Ribbeck. (f) The winter rapeseed field southeast of Ribbeck, where several of this study's samples were found (AKM01, AKM05).

MINERALOGY

The broken surfaces of the stones perfectly show the brecciated texture of Ribbeck (Figure 2; Figures S1 and S3). Large light-colored fragments are easily recognized in hand specimens and are embedded in a dark-gray groundmass. Thus, obviously, Ribbeck is a breccia consisting of a mixture of different lithologies. This textural characteristic is also observable in polished thin sections (Figure 5). Many of the light-colored large clasts are millimeter-sized fragments of single crystals indicating fragmentation of extremely coarse-grained precursor rocks.

The aubrite breccia Ribbeck consists of major (76 ± 3 vol%), nearly FeO-free enstatite ($En_{99.1}$ $Fs_{<0.04}Wo_{0.9}$) with a significant abundance (15.0 ± 2.5 vol %) of albitic plagioclase ($Ab_{95.3}$ $An_{2.0}Or_{2.7}$ with an An variation between 0.16 and 5.7 mole%), minor forsterite (5.5 ± 1.5 vol%; $Fo_{99.9}$) and 3.5 ± 1.0 vol% of opaque phases (mainly sulfides and metals). Traces of nearly FeO-free diopside ($En_{53.2}Wo_{46.8}$), K-feldspar ($Ab_{4.6}Or_{95.4}$) and of a S-bearing K-feldspar-like phase were found (Table 1). It is unclear whether the S in the latter phase occurs in an elemental state or whether it is present as an oxide (SO_3^{2-}). As an oxide, the SO_3 concentration would
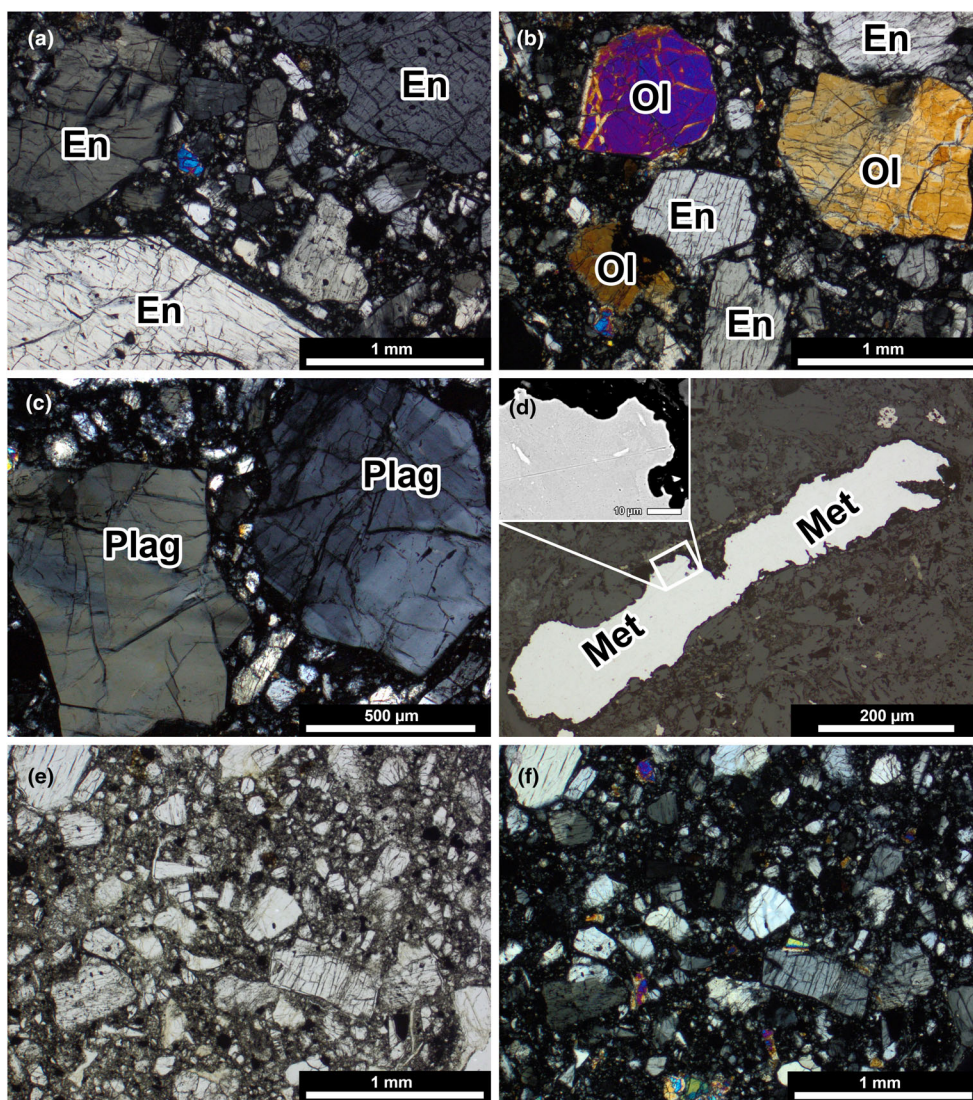
FIGURE 5. The brecciated texture of Ribbeck in thin section: (a) Fine-grained clastic matrix between millimeter-sized enstatite crystals (En); polarized light, crossed nicols. (b) Large fragments of olivine (Ol) and enstatite (En) embedded in a fine-grained clastic matrix; the yellowish olivine shows abundant planar deformation features (compare with "Shock Metamorphism" chapter); polarized light, crossed nicols. (c) Two large plagioclase (Plag) fragments with slightly anomalous interference colors; polarized light, crossed nicols. (d) Fragment of the largest metal (Met) found in the clastic matrix of the studied thin sections; reflected light; insert: BSE image of Ni-rich metal grains (white) inside texturally inhomogeneous kamacite. (e) Fine-grained clastic area in the brecciated aubrite; plane polarized light. (f) Same area as in (e); crossed nicols.

be ~3.3 wt%. Some typical mineralogical features are presented in Figures 5–7.

Metals, schreibersite and sulfides (or their alteration products) contribute to about 3.5 ± 1.0 vol% (Figure 7). Ribbeck also contains a minor abundance of metallic Fe, Ni similar to those described by Watters and Prinz (1979), Casanova et al. (1993), and Keil (2010) for other aubrites. However, the metal analyzed in this study has an extremely low mean Si concentration of 0.11 wt% and 2–4 wt% Ni (Table 2). Within the largest metal aggregate, small particles of a Ni-rich metal (~55 wt% Ni, 0.3 wt% Co, probably taenite or tetrataenite) were found in kamacite (Figure 5d). The kamacite is texturally inhomogeneous considering the Ni- and Co-distributions (insert in Figure 5d), leading to slightly variable gray tones in the BSE image. Schreibersite has 26.7 wt% Ni and 57.2 wt% Fe (Table 2). Among the sulfides, troilite is quite abundant. Two populations of troilite appear to exist: one is Ti rich (5–7 wt%; Table 2) and the other has low Ti concentrations (0.1–2.2 wt%; Table 2). However, we cannot completely rule out that a continuous range of troilite compositions exists. Djerfisherite ($K_3(Na,Cu)(Fe,$

TABLE 1. Mean chemical composition of the silicate phases in Ribbeck obtained by electron microprobe analysis.

	Olivine ($n = 20$)	Low-Ca Px ($n = 313$)	High-CaPx ($n = 2$)	Plag ($n = 21$)	K-Fsp ($n = 2$)	K-Fsp-like ($n = 5$)
SiO_2	41.9	59.1	55.9	67.1	65.0	64.6
TiO_2	<0.01	<0.02	0.45	<0.01	0.08	<0.02
Al_2O_3	<0.01	0.05	0.35	19.3	18.3	16.2
Cr_2O_3	<0.01	<0.01	0.15	<0.01	<0.01	<0.01
FeO	0.02	0.03	<0.02	<0.03	<0.04	0.06
MnO	<0.01	<0.02	n.d.	<0.01	<0.05	<0.03
MgO	57.9	40.1	19.2	<0.02	n.d.	<0.02
CaO	0.05	0.51	23.4	0.44	n.d.	0.28
Na_2O	<0.01	<0.02	0.45	11.4	0.51	2.10
K_2O	<0.01	<0.01	n.d.	0.49	15.9	16.2
P_2O_5	<0.01	<0.01	n.d.	<0.01	n.d.	<0.03
S	<0.02	<0.02	<0.02	<0.02	0.04	1.3
Total	99.96	99.58	99.94	98.84	99.93	100.82
Fo	99.9					
En		99.1	53.2 ± 0.1			
Wo		0.9	46.8 ± 0.1			
Ab				95.3	4.6 ± 0.8	
Or				2.7	95.4 ± 0.8	

Note: All data in wt%.

Abbreviations: K-Fsp, K-feldspar; *n*, number of analyses; n.d., not detected; Plag, plagioclase; Px, pyroxene.

$Ni)_{12}S_{14}$; Clay et al., 2014; Fuchs, 1966; Keil, 2010; McCoy et al., 2000; Wilbur et al., 2024) is also quite abundant, having 5–10 wt% K and 1–2 wt% Cl. Two types of alabandite (Mn,Fe)S have been found. The most abundant variety contains about 5 wt% Mg and 11–20 wt % Fe, while the other type is poor in Mg (<1 wt%; Table 2). Only a few grains of oldhamite (CaS) exist in the studied thin sections. Most oldhamites are already in the process of weathering, indicated by textural, lattice-like features (Wilbur et al., 2022) and low analytical totals. One of the forming alteration products is a Ca-rich phase that could be portlandite ($Ca(OH)_2$; Figure 9b). The degree of oldhamite weathering is highly variable on a centimeter scale, as demonstrated by comparing Figure 9b,d. This has also been reported for the Neuschwanstein E chondrite meteorite fall (Zipfel et al., 2010).

Among the opaque components, two other phases also appear to have been altered in the wet environment during the 6 days before the studied samples were found. Based on the high Cr concentration ($\sim$31 wt%), one of these phases could be related to cronusite ($Ca_{0.2}CrS_2 \times H_2O$; Figure 7d; Table 2). This phase appears to be an alteration product of caswellsilverite ($NaCrS_2$). However, daubréelite ($FeCr_2S_4$) and brezinaite (Cr_3S_4; Bunch & Fuchs, 1969) cannot completely be ruled out as possible other precursor (parental) phases before alteration. The other altered phase could have been a Ti-rich sulfide (Figure 7a; Table 2) before the terrestrial aqueous alteration that occurred over the 6 days. Although these two phases are heavily altered (resulting in low analytical totals of about 80 wt%; Table 2), we observed no reaction zones around the grains nor veins within neighboring minerals filled with secondary alteration products (Figure 7a,d).

Namely, the phases caswellsilverite, heideite ([Fe, $Cr]_{1+x}[Ti,Fe]_2S_4$), keilite ([Fe,Mn,Mg,Ca,Cr]S), and schöllhornite ($Na_{0.3}CrS_3 \times 3H_2O$) (e.g., Keil, 2007; Keil & Brett, 1974; Okada & Keil, 1982; Okada et al., 1985), which have been reported in the meteorite database (The Meteoritical Bulletin, 2024) and by Hamann et al. (2024), were not observed in this study, but we cannot rule out that the altered Ti-rich sulfide results from the terrestrial destruction of heideite.

Shock Metamorphism

The studied thin section of the brecciated aubrite Ribbeck clearly shows that the rock is a complex breccia (e.g., Figure 5 and Figure S3). In order to determine the shock degree of a bulk rock breccia, the fragment with the lowest degree of shock has to be considered. Large olivine grains in the present thin sections were checked for shock features. All large olivines show planar fractures and/or weak mosaicism (Figure 8a). Thus, Ribbeck has a shock degree of S3 (U-S3) considering previous studies concerning the degree of shock metamorphism (Bischoff, Schleiting, et al., 2019; Bischoff & Stöffler, 1992; Rubin et al., 1997; Stöffler et al., 1991, 2018). Since the brecciated character of Ribbeck is easily detectable in the hand specimen, it is also clearly visible in thin sections (Figure 5) and also found at the fine-grained scale in the matrix
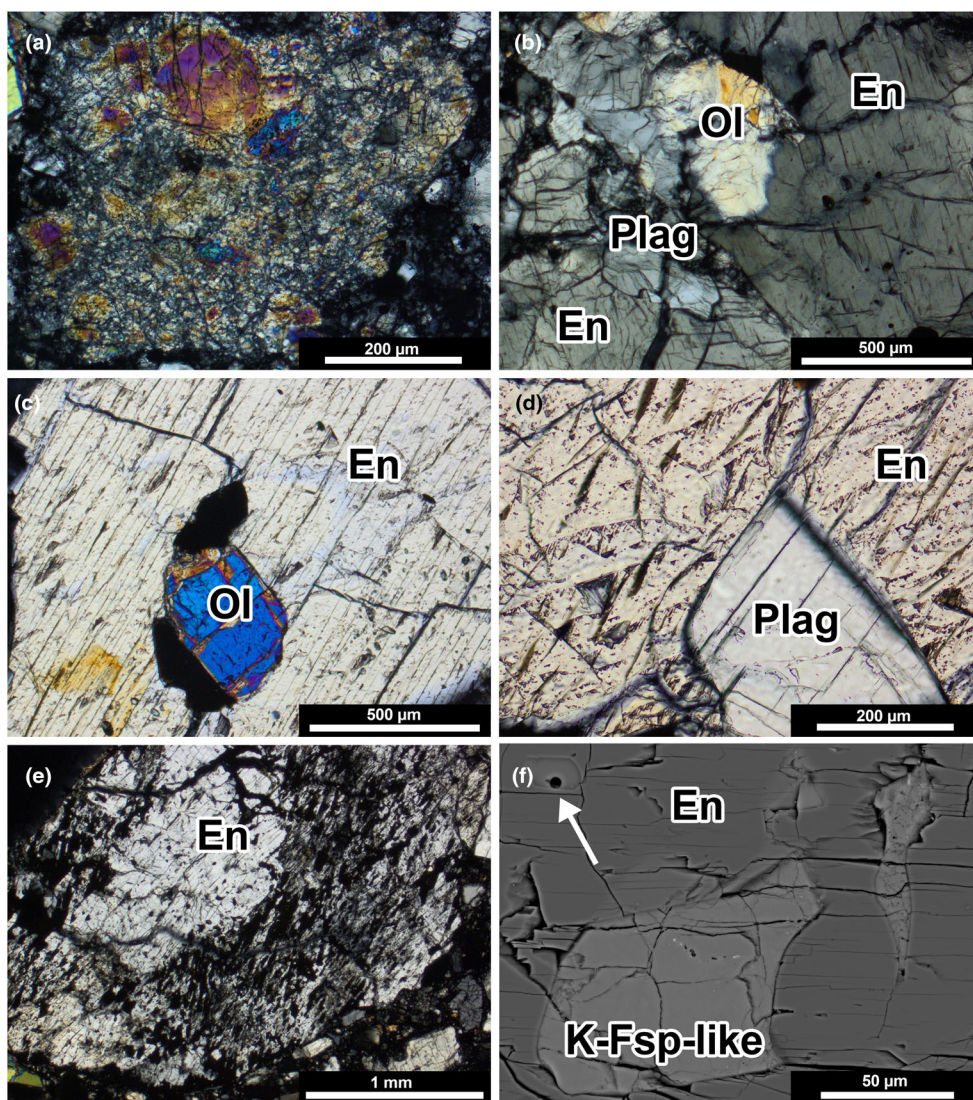
FIGURE 6. (a) Fine-grained fragmented olivine. The olivine also shows mosaicism (see below in "Shock Metamorphism" chapter; compare Figure 8). (b) Olivine (Ol) and plagioclase (Plag) enclosed in enstatite (En). (c) Olivine (Ol) grain enclosed in enstatite (En). (d) Intergrowth of plagioclase (Plag) and enstatite (En). (e) A several millimeter-sized enstatite-rich clast strongly resembling a radial pyroxene chondrule with an enstatite core (En). (f) Two non-stoichiometric K-feldspar-like (K-Fsp-like; light gray) grains (Table 1) and K-feldspar-normative melt inclusion (arrow) in enstatite (En). All figures are taken in polarized light, crossed nicols, except for (f), which is a BSE image.

(Figure 8d) All components contain abundant micro-cracks (Figure 8d). Individual clasts certainly exist that have a higher degree of shock metamorphism than S3 (U-S3) and show mosaicism (Figure 8b). Strong twinning is observed for Ca-pyroxene (Figure 8c). The unusual, anomalous interference colors of albitic plagioclase (Figure 5c) may also derive from shock metamorphism. In addition, areas with shock-darkened silicates were observed. We also detected thin impact melt veins (Figure 8e) and small shock-melted areas (Figure 8f), which indicate a complex impact-related history. Since the melt veins and areas are within the fine-grained clastic

areas, they must have been formed after early brecciation and re-accretion. Similar impact melts were also found in Bishopville (Wilbur et al., 2022).

Terrestrial Weathering

The Ribbeck meteorite fell when the surface in the strewnfield was covered with snow, which melted within the next few days. The first samples were found 4 days after impact with Earth. In the time between the fall event and recovery (6 days for the fragment studied here), the samples were affected by water activities, which caused
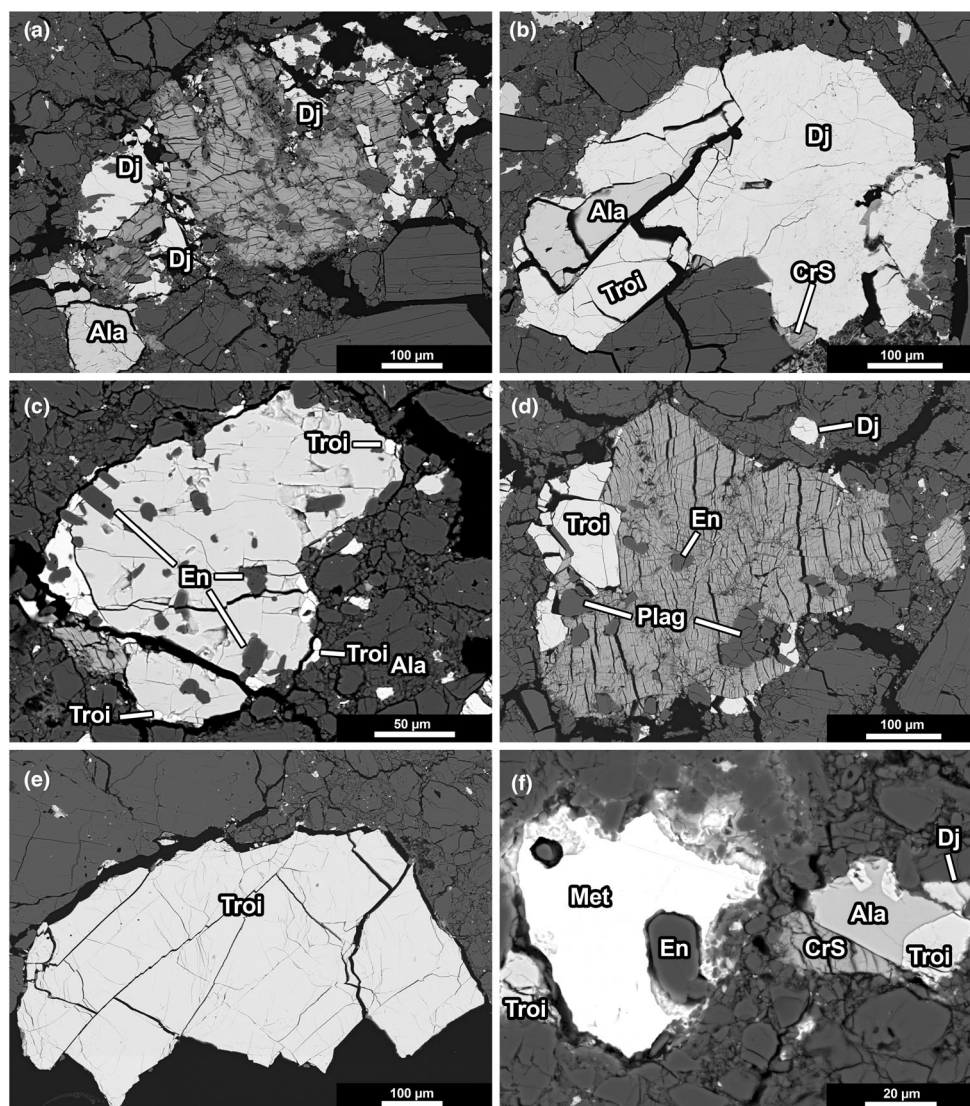
FIGURE 7. Sulfide- and metal-bearing components in Ribbeck: (a) Complex aggregate mainly consisting of a weathered Ti(+Fe, Ca,Cr)-rich sulfide (gray; Table 2) and in paragenesis with djerfisherite (Dj) and alabandite (Ala). (b) Paragenesis of djerfisherite (Dj), alabandite (Ala), troilite (Troi) and a Cr-rich sulfide (CrS). (c) Alabandite (Ala) with inclusions of enstatite (En) and djerfisherite (Dj) and troilite (Troi) at the borders. (d) Weathered Cr-rich sulfide (perhaps former caswellsilverite (or daubréelite (?); gray); Table 2) with inclusions of enstatite (En) and plagioclase (Plag) in paragenesis with djerfisherite (Dj) and troilite (Troi). (e) The largest troilite (Troi) found in the studied thin section. (f) One of the rare metal (Met; partly weathered at the rim) grains together with alabandite (Ala), troilite (Troi), djerfisherite (Dj) and a Cr-rich sulfide (CrS). BSE-images.

visible terrestrial weathering especially of the metals (see also Figure 7f) and sulfides, resulting in the brownish appearance of rock pieces (Figure 9a and Figure S2f) and the partial destruction of certain sulfides (especially oldhamite; Figure 9b–d), which probably also contributed to the fragments' pungent H_2S odor upon recovery. The main silicates enstatite, forsterite and plagioclase are still intact. Thus, we suggest that the weathering degree of individual stones should be W0/1 or W1 (Wlotzka, 1993).

Oxygen Isotopes

The O-isotope compositions of two small chips from the 4.3 g specimen of Ribbeck are listed in Table 3. The values of $\delta^{17}O$, $\delta^{18}O$ and $\Delta'^{17}O_{0.528}$ for the two samples are 2.632, 5.093, −0.054 and 2.704, 5.222, −0.050‰, respectively, and similar to data of the standard San Carlos.

The data fall close to the data point for the bulk silicate Earth (BSE) and are also similar to those of

TABLE 2. Chemical composition of kamacite and various types of sulfides in Ribbeck obtained by electron microprobe analysis.

	Kamacite ($n = 7$)	Troilite ($n = 8$)	Ti-Troilite ($n = 26$)	Weathered Cr-rich phase ($n = 7$)	Mg-Alabandite ($n = 15$)	Alabandite ($n = 2$)	Weathered Ti-rich phase ($n = 7$)	Djerfisherite ($n = 21$)	Oldhamite ($n = 3$)	Schreibersite ($n = 3$)
Na	<0.01	0.04	<0.01	0.58	0.05	0.07	0.10	0.19	0.13	<0.03
Mg	<0.01	0.03	<0.02	0.33	5.6	0.77	0.60	0.06	0.31	<0.02
F	n.d.	n.d.	<0.01	0.04	<0.02	<0.02	0.06	n.d.	0.07	n.a.
Al	<0.03	n.d.	n.d.	<0.02	<0.01	<0.01	0.05	n.d.	n.d.	<0.03
Si	0.11	0.05	<0.02	0.21	0.07	0.03	0.22	n.d.	0.06	0.11
K	<0.02	<0.02	<0.01	0.58	<0.01	n.d.	0.20	8.6	<0.01	n.d.
Ca	<0.03	0.14	n.d.	5.3	0.17	0.12	5.4	n.d.	53.1	0.12
S	<0.01	35.8	37.0	40.7	38.9	35.9	35.6	33.2	42.8	<0.01
P	<0.02	n.d.	n.d.	<0.01	n.d.	n.d.	<0.03	n.d.	<0.01	15.8
Cl	n.d.	n.d.	<0.01	0.07	<0.01	n.d.	<0.01	1.35	0.10	n.a.
Ti	<0.02	1.19	5.5	2.51	0.03	<0.02	16.9	<0.02	<0.01	n.d.
Cr	<0.01	0.22	0.44	31.0	0.15	0.20	7.1	0.16	n.d.	<0.02
Mn	<0.02	0.87	0.04	0.08	40.1	46.0	<0.03	<0.02	0.92	0.05
Fe	96.2	60.8	55.5	0.50	14.0	13.7	7.6	54.7	0.08	57.2
Co	0.51	0.06	0.07	<0.01	0.04	<0.01	<0.01	0.09	n.d.	n.a.
Ni	2.83	0.07	<0.01	0.12	0.04	n.d.	2.03	0.73	n.d.	26.7
Total	99.83	99.29	98.64	82.08	99.20	96.85	75.94	99.02	97.60	100.09

Note: All data in wt%. Some of these are already heavily altered (Figures 7 and 9), resulting in low totals, especially of a Cr-rich phase (perhaps cronusite) and an unknown Ti-rich phase.
Abbreviations: n, number of analyses; n.a., not analyzed; n.d., not detected.
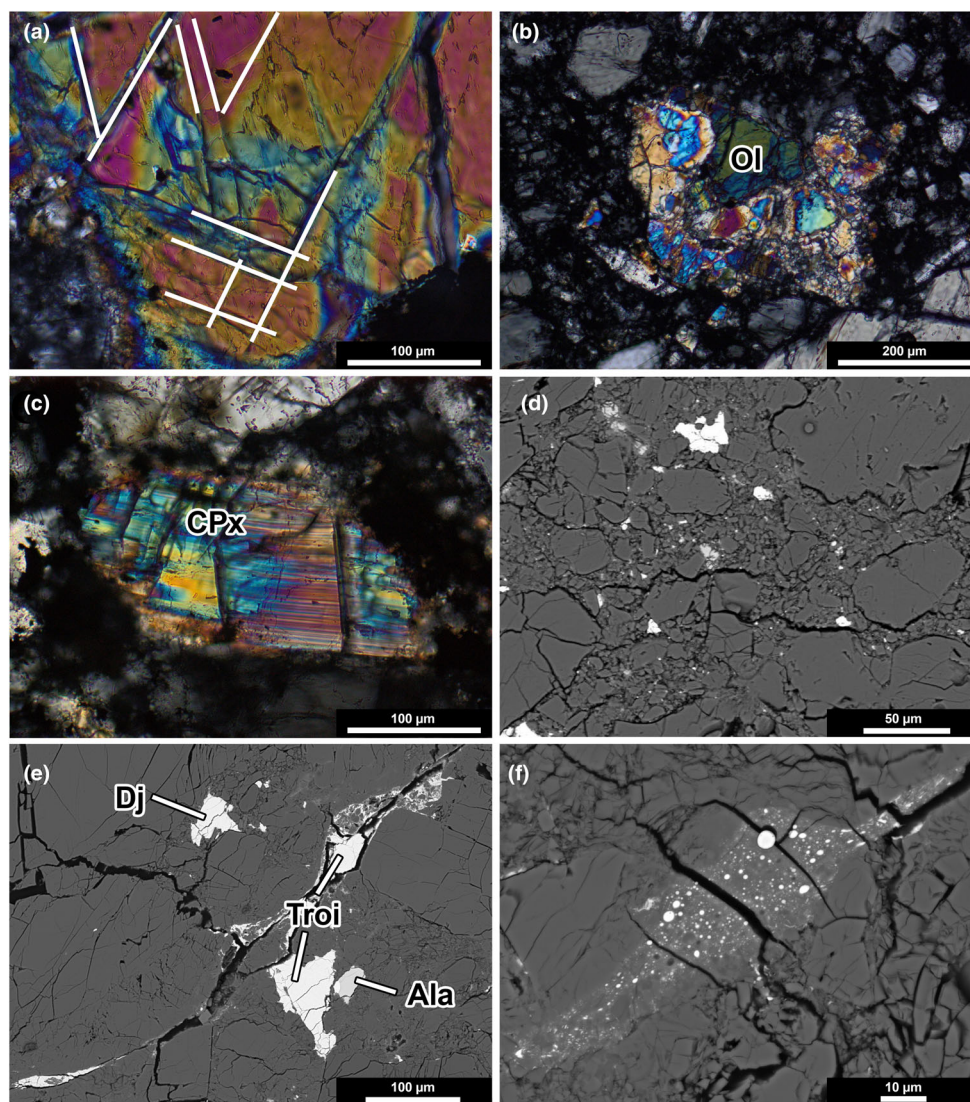
FIGURE 8. (a) Olivine with planar fractures indicated by white lines. (b) A shocked fragment containing mosaicized olivine; image in polarized light, crossed nicols. (c) Severe shock twinning of Ca-pyroxene; polarized light, crossed nicols. (d) The typical brecciated texture within the fine-grained parts of Ribbeck. (e) Thin shock vein in the fine-grained part of Ribbeck with abundant troilite (Troi); also visible are alabandite (Ala) and djerfisherite (Dj). (f) Melt area with abundant Fe-sulfide spherules. Images in (d) to (f) taken in backscattered electron mode (BSE).

other aubrites and E chondrites (Figure 10, e.g., Wilbur et al., 2022 and the The Meteoritical Bulletin, 2024).

Bulk Chemical Characteristics

For most elements, the chemical composition of Ribbeck (Table 4) is close to the composition of the recently analyzed Bishopville aubrite and is also similar to the Aubres (from which the name "aubrites" derives), Norton County, and other aubrites (Barrat, Greenwood, et al., 2016; Lodders & Fegley, 1998; Wilbur et al., 2022).

Considering the bulk composition of aubrites, Ribbeck has low abundance of REE with a strong positive Eu anomaly. In this respect, the new fall is very similar to Bishopville (Figure 11). The positive Y-anomaly is remarkable, but often observed in aubritic and EC silicates (Barrat et al., 2014, 2023; Barrat, Greenwood, et al., 2016). Considering the analyzed residues after leaching (compare Barrat et al., 2023) Ribbeck has the lowest abundance of the heavy REE (Figure 11b). The marked differences between the compositions of the bulk and the residue are due to the presence of sulfides rich in elements that are usually lithophile in less reduced meteorites, and removed by the leaching step (e.g., REEs, Ti, Zr, U).

FIGURE 9. (a) Small (6.5 mm) fragment of Ribbeck found 6 days after impact with Earth, already showing significant effects of terrestrial alteration. (b) BSE image of a small oldhamite showing significant lattice-like features of terrestrial alteration at the boundaries and on cracks. The alteration product could be portlandite, which is often observed around oldhamites in aubrites and E chondrites (Keil, 2010; Zipfel et al., 2010). (c) La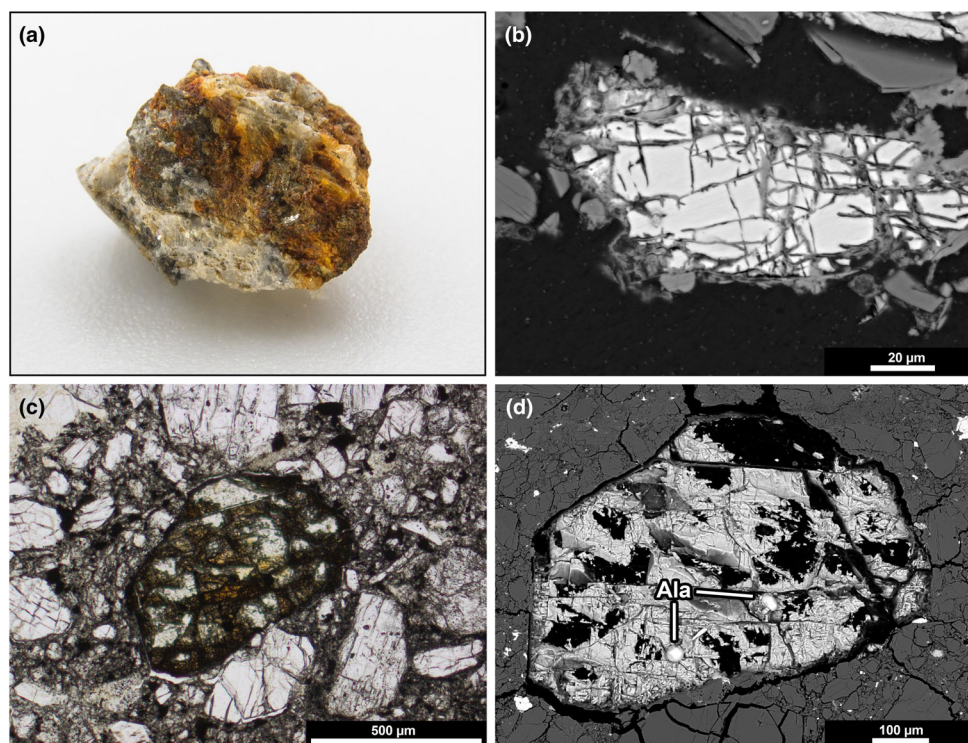rge altered oldhamite-rich area in plane polarized light. (d) Photo of the same object as in (c) taken with backscattered electrons (BSE) showing the heavily altered oldhamite with some inclusions of alabandite (Ala).

TABLE 3. Oxygen isotope composition of two aliquots from the Ribbeck achondritic breccia (sample AKM01) and four data points from the standard San Carlos given in ‰.

Sample	Mass (mg)	$\delta^{17}O$	$\delta^{18}O$	$\Delta'^{17}O_{0.528}$
Ribbeck-1	2.150	2.632	5.093	−0.054
Ribbeck-2	2.174	2.704	5.222	−0.050
Mean:	2.162	2.668	5.158	−0.052
SanCarlos-1	2.029	2.652	5.128	−0.053
SanCarlos-2	2.080	2.710	5.249	−0.058
SanCarlos-3	2.150	2.711	5.253	−0.059
SanCarlos-4	2.119	2.743	5.273	−0.038

Titanium Isotopes

The nucleosynthetic Ti isotope data for Ribbeck are listed in Table 5. The Ti isotope composition of Ribbeck is consistent with literature data of aubrites (Zhang et al., 2012) and slightly negative in $\varepsilon^{50}Ti$ relative to Earth (Figure 12). Thus, the Ti isotope data indicate that the new Ribbeck meteorite originated in the NC (non-carbonaceous meteorite) reservoir within the inner solar system and belongs to the aubrite meteorite group.

Noble Gas Composition

Noble gas concentrations and isotopic compositions measured in Ribbeck are given in Tables 6–8. The Ne data shows no evidence of a trapped component and, thus, Ne and He in Ribbeck are purely cosmogenic, apart from $^4He_{rad}$. We can exclude the presence of a solar wind component and conclude that Ribbeck is not a regolith breccia, but a fragmental breccia. Also, the results show no indication for SCR-Ne (Ne produced by solar cosmic rays resulting in low cosmogenic $^{21}Ne/^{22}Ne$ ratios typically below ∼0.8; e.g. Wieler et al., 2016), which implies that the analyzed sample does not originate from the uppermost few cm below the meteoroid surface as the penetration depth of SCRs is low, mostly ≤4 cm (e.g., Garrison et al., 1995; Hohenberg et al., 1978; Wieler et al., 2016). The $^{36}Ar/^{38}Ar$ ratio reveals a trapped Ar component in addition to Ar_{cos} and $^{40}Ar_{rad}$. The origin of the trapped Ar is, however, impossible to resolve since the Ar isotopic compositions of the trapped components are too similar
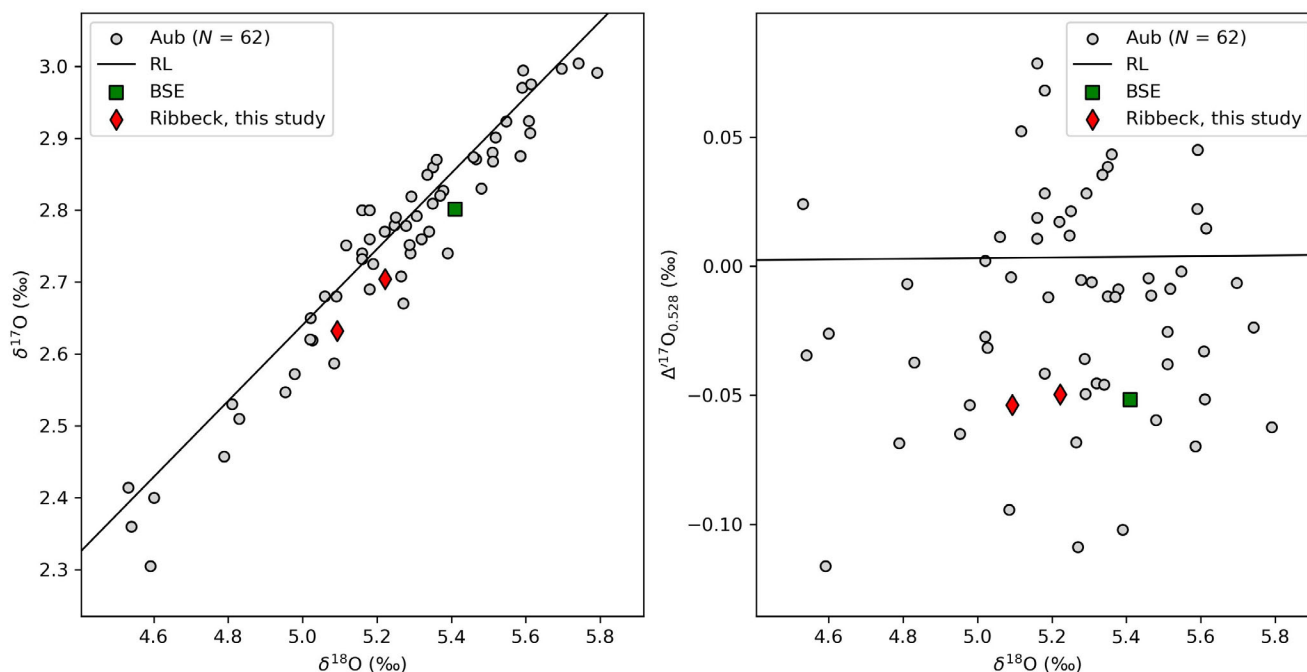
FIGURE 10. Triple oxygen isotope compositions (δ^{17}O vs. δ^{18}O and Δ'^{17}O vs. δ^{18}O) of two individual chips of Ribbeck. The composition of aubrites, compiled from the Meteoritical Bulletin Database, as well as the composition of the bulk silicate Earth (BSE, Peters et al., 2021) are shown for comparison. The reference line (RL) of slope 0.528 is plotted for reference.

and the results are consistent with both Q and air composition. There is only very little trapped Kr and Xe in Ribbeck, consistent with earlier observations in aubrites (Busemann & Eugster, 2002; Lorenzetti et al., 2003). Thus, the measured Kr and Xe isotope compositions show strong relative contributions from spallogenic Kr_{cos} and Xe_{cos}, and neutron-capture of Br on ^{80,82}Kr.

Shielding Conditions and CRE Ages

Possible shielding conditions and production rate ranges P_x constrained by the model as well as cosmogenic noble gas concentrations and calculated CRE ages T_x are given in Table 9. In agreement with the results of the radionuclide data (see section below "Constraints on Preatmospheric Radius and Shielding Depths by Cosmogenic Radionuclides"), a preatmospheric meteoroid radius of ≤ 10 cm is excluded. Additionally, possible sample depth ranges within the meteoroid constrained by noble gases (8–14 cm) and radionuclides (3–10 cm) overlap. However, the presence of excess ^{80,82}Kr from n-capture of Br with a $(^{80}Kr/^{82}Kr)_n = 2.5 \pm 1.2$ in Ribbeck (within the typical range expected for neutron capture derived Kr; Marti et al., 1966) suggests that this sample must have been in slightly larger depth (typically depths of 20–30 cm are given for efficient n-capture; Eberhardt et al., 1963) for significant time where secondary neutrons were sufficiently moderated to enable this reaction.

We observe some variation among the CRE ages determined based on the different cosmogenic noble gas isotopes. The T_{38} age range is low compared to T_3 and T_{21}. The $^{38}Ar_{cos}$ concentration is very sensitive to target element concentrations, here mainly Ca. Indeed, the Ca content given in Table 4 is high for aubrites (1.2 wt%), responsible for the relatively low T_{38} age. For example, a Ca content of ~0.35 wt% (also in a typcial range for other aubrites; compare e.g. with Lorenzetti et al., 2003) would result in a T_{38} age in the range of the T_3 and T_{21} age. However, such large variation in Ca concentration is not to be expected in 0.75 g homogenized powder (AKM01). Note that the abundance of K is not considered in the model which would decrease T_{38} even more. Although more similar to each other, the T_3 age range is still slightly lower than the T_{21} age range. Lower T_3 ages can indicate a noble gas loss due to heating, e.g., during atmospheric entry, which preferentially affects the lighter noble gases. However, the Ribbeck data plots well on the trend of other aubrites in a cosmogenic ^{3}He/^{21}Ne versus ^{22}Ne/^{21}Ne diagram ("Bern plot", cf. Figure 3 in Lorenzetti et al., 2003), suggesting no significant ^{3}He loss. More likely, the relatively low T_3 age results from an overestimation of the ^{3}He production rate in the model. For example, Dalcher et al. (2013) report a divergence between modeled and measured chondrite data (cf. Figure 1 in their study) that causes a discrepancy of ~15% in the $(^3$He/^{21}Ne$)_{cos}$ ratio for a $(^{22}$Ne/^{21}Ne$)_{cos}$ ratio of ~1.115 as measured in

TABLE 4. Major and trace element abundances of the Ribbeck aubrite breccia (sample AKM01).

Element	Units	Ribbeck Bulk	Bishopville Bulk	Norton County Bulk	Ribbeck Residue	Bishopville Residue
Si	wt%	25.9[a]				
Al	wt%	1.22			1.11	
Fe	wt%	0.78[a]				
Mg	wt%	21.02			21.38	
Na	wt%	1.13[a]			0.51	
Ca	wt%	1.20			0.35	
P	$\mu g\,g^{-1}$	96			99	
K	$\mu g\,g^{-1}$	1211			529	
Sc	$\mu g\,g^{-1}$	12.0	4.80	7.33	8.33	4.26
Ti	$\mu g\,g^{-1}$	840	269	302	144	92
V	$\mu g\,g^{-1}$	8.90	6.21	9.62	0.630	0.767
Cr	$\mu g\,g^{-1}$	559			174	
Mn	$\mu g\,g^{-1}$	1600	927	1300	61.4	87
Co	$\mu g\,g^{-1}$	5.3			1.25	
Ni	$\mu g\,g^{-1}$	170			35.4	
Cu	$\mu g\,g^{-1}$	12.7			3.59	
Zn	$\mu g\,g^{-1}$	1.14			0.13	
Ga	$\mu g\,g^{-1}$	0.048			0.010	
Rb	$\mu g\,g^{-1}$	3.32	1.470	0.357	0.880	1.205
Sr	$\mu g\,g^{-1}$	12.93	10.51	1.394	8.49	11.08
Y	$\mu g\,g^{-1}$	0.823	0.538	2.561	0.142	0.160
Zr	$\mu g\,g^{-1}$	13.47	3.021	0.684	3.46	1.02
Nb	$ng\,g^{-1}$	89.6	26.8	27.6	43.9	14.8
Mo	$ng\,g^{-1}$	55.9			23.6	
Cs	$ng\,g^{-1}$	198	40.8	24.4	66.2	27.7
Ba	$ng\,g^{-1}$	6272	3654	326	4681	3820
La	$ng\,g^{-1}$	229	92.2	326	14.9	5.62
Ce	$ng\,g^{-1}$	344	151	1105	24.4	7.07
Pr	$ng\,g^{-1}$	39.5	22.0	201	3.28	1.11
Nd	$ng\,g^{-1}$	186	111	1045	13.2	6.12
Sm	$ng\,g^{-1}$	62.9	36.5	329	5.12	3.09
Eu	$ng\,g^{-1}$	124	50.3	37.7	22.9	40.8
Gd	$ng\,g^{-1}$	82.9	57.4	435	9.75	8.44
Tb	$ng\,g^{-1}$	15.4	11.4	76.7	2.29	1.95
Dy	$ng\,g^{-1}$	106	81.0	498	15.3	16.7
Ho	$ng\,g^{-1}$	24.0	18.7	108	3.78	4.49
Er	$ng\,g^{-1}$	72.3	57.5	311	11.7	15.0
Yb	$ng\,g^{-1}$	84.5	63.8	281	14.2	20.2
Lu	$ng\,g^{-1}$	13.8	10.6	41.4	2.93	3.61
Hf	$ng\,g^{-1}$	441	111	23.4	220	64.0
Ta	$ng\,g^{-1}$	19.0			11.6	
Pb	$ng\,g^{-1}$	91.2	126	45.3	25.8	2.3
Th	$ng\,g^{-1}$	65.6	27.7	6.80	6.75	3.53
U	$ng\,g^{-1}$	11.3	3.29	7.91	2.66	0.32

Note: Data for Bishopville and Norton County for comparison from Barrat, Greenwood, et al. (2016).
[a]From microprobe analyses.

Ribbeck. Lowering P_3 accordingly would result in a T_3 that agrees with the T_{21}. We consider the T_{21} age most reliable as $^{21}Ne_{cos}$ is less affected by heating, systematic errors in the model, and target element heterogeneities compared to cosmogenic ^{3}He and ^{38}Ar. Thus, our preferred CRE age for Ribbeck based on the analyzed sample and applied methods is ~55–62 Ma.

U/Th-He and K-Ar Gas Retention Ages

Aubrites formed very early, i.e., within a few Ma after the formation of calcium-aluminium-rich inclusions based on the I-Xe, Pb–Pb, and Mn-Cr chronometers (Keil, 2010). The K-Ar age determined for Ribbeck (T_{40} = ~3.3–3.7 Ga; Table 10) suggests a later closure of
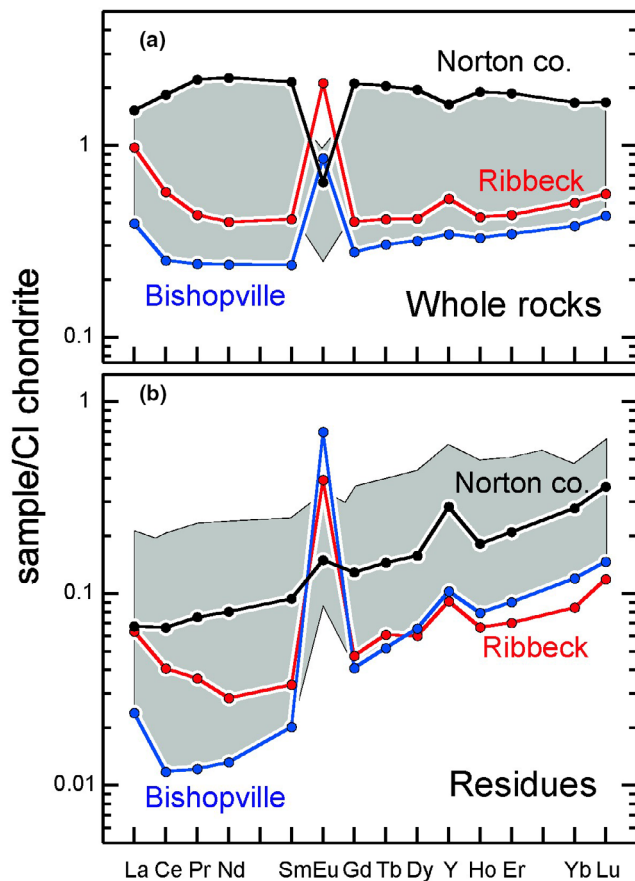
FIGURE 11. (a) Whole-rock composition of Ribbeck in comparison with the compositions of Norton County and Bishopville (Barrat, Greenwood, et al., 2016), which both represent the chemical endmembers among the variety of aubrites. All data from aubrites plot within the gray field. (b) Composition of the residues of the three aubrites showing positive Eu and Y anomalies. The gray field represents all variations of the compositions of all aubritic residues studied (Barrat, Greenwood, et al., 2016).

TABLE 5. Nucleosynthetic Ti isotope data for Ribbeck.

Sample	n^a	$\varepsilon^{46}Ti$	2 SE^b	$\varepsilon^{48}Ti$	2 SE^b	$\varepsilon^{50}Ti$	2 SE^b
Ribbeck	10	−0.01	0.06	0.00	0.02	−0.12	0.06
Forest Vale[c]	6	−0.08	0.11	−0.03	0.05	−0.56	0.08
BHVO-2	8	−0.08	0.07	0.01	0.03	0.01	0.08

[a]Number of measurements.
[b]Isotopic values are averages of repeats. Uncertainties are given in 2 SE (SE = SD/$\sqrt{n}$).
[c]Titanium analysis by Williams (2015), re-measured in this study.

the K-Ar system, indicating that Ribbeck's parent body experienced a relatively late severe event that reset the K-Ar chronometer. The U/Th-He age (T₄) is with ~2.3–2.5 Ga younger than the K-Ar age which implies

(multiple) smaller resetting events, e.g., induced by impacts, on the Ribbeck parent body after the closure of the K-Ar system (Table 10). Based on the brecciated texture of Ribbeck the effects of severe impact activities on the parent body are obvious. Even after large-scale brecciaton further impact processes are required to explain the formation of small shock melted areas and shock veins in the fine-grained clastic matrix of Ribbeck (Figure 8e,f).

Fourier Transform Infrared Spectroscopy

The IR spectrum of the analyzed Ribbeck bulk sample contains several reflectance peaks (Reststrahlenbands, RB) and shoulders in the mid-infrared wavelength range between 6 and 18 μm (Figure 13). These peaks are approximately at 6.43, 7.11, 8.25, 9.00, 9.29, 9.85, 10.16, 10.45, 10.74, 11.07, 11.51, 12.11, 13.83, 14.39, 15.48 and 17.33 μm. The shoulders are underlying peaks of which two are visible at ~8.8 and ~16.5 μm. The region of the Christiansen feature (CF, global characteristic minimum) contains two minima with comparable reflectance divided by the weak peak at 8.25 μm. The first CF minimum is at 8.15 μm and the second is at 8.49 μm. A clear Transparency feature was not observed in the spectrum, indicating a mean grain size well above ~25 μm.

Raman Spectroscopy

Raman spectroscopy measurements were taken especially on the K-like feldspar phase having significant concentrations of S (Table 1), as well as on the 'weathered Cr-rich phase' and 'unknown Ti-rich' phases, which both can be characterized by low analytical totals of about 80 wt% (Table 2). These two phases are certainly related to sulfides, but a precise mineral identification is difficult based on the chemical compositions. The Raman spectra (Figure S4) of the feldspar-like phase gives us an unambiguous feldspar spectrum. Although the main peaks at 284 cm⁻¹, 326 cm⁻¹, and the typical double peak at 463 cm⁻¹/500 cm⁻¹ shift a bit to lower wavenumbers compared to those of orthoclase (Mernagh, 1991). The sulfides show typical spectra with a high signal to noise ratio (compare Avril et al., 2013; Figure S4). However, the resulting Raman shifts are an indication that these phases are related to sulfides even they have analytical totals of only 80 wt%. Even though, water bands could not clearly be identified. However, a laser sensitivity could be observed at least for the 'unknown Ti-rich phase' similar to that reported by Weber et al. (2017).

Measurements of Density and Magnetic Properties

The density of several Ribbeck fragments were measured using several methods described in detail in the
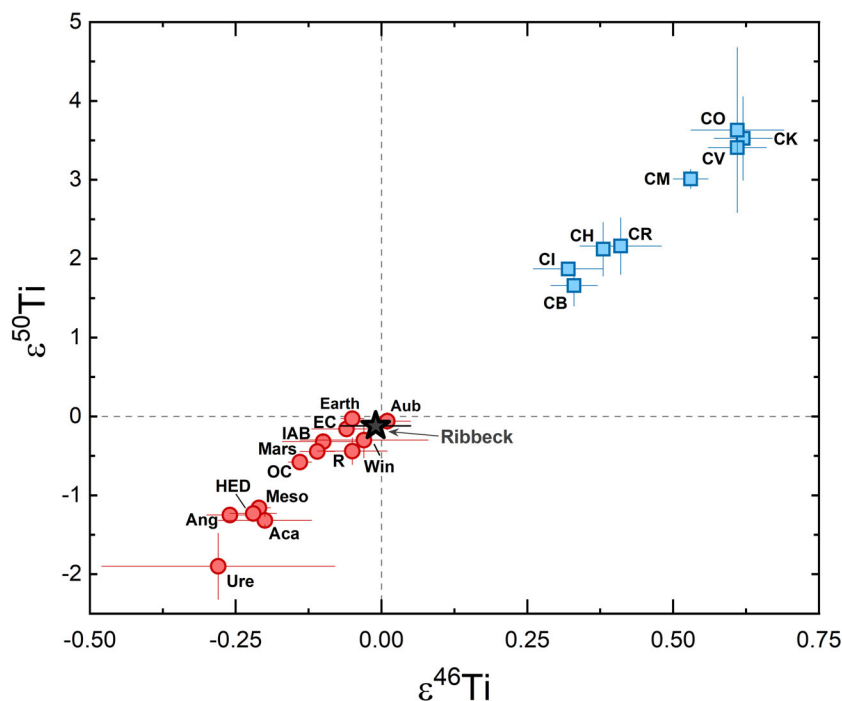
FIGURE 12. The Ti isotope composition of Ribbeck (black star) is consistent within the compositions of other aubrites. Thus, it belongs to the category of non-carbonaceous chondrites, which are assumed to have formed from inner solar system material. The averages and corresponding uncertainties are taken from the compilation of Rüfenacht et al. (2023). Aca, acapulcoites; Ang, angrites; Aub, aubrites; CC, carbonaceous chondrites; EC, enstatite chondrites; IAB sil, IAB silicates; Lod, lodranites; Meso, mesosiderites; Win, winonaites.

TABLE 6. Sample mass used for the Ribbeck noble gas analysis, He and Ne concentrations (in 10^{-8} cm^3 STP g^{-1}) and isotopic ratios. Also given are the shielding-dependent cosmogenic isotope ratios.

Mass (mg)	^{4}He	^{3}He/^{4}He $\times 10^4$	^{20}Ne	^{20}Ne/^{22}Ne	^{21}Ne/^{22}Ne	$(^{22}$Ne/^{21}Ne$)_{cos}$	$(^3$He/^{21}Ne$)_{cos}$
13.822 ± 0.027	1432.4 ± 4.2	648.5 ± 3.3	25.15 ± 0.22	0.8250 ± 0.0050	0.8970 ± 0.0043	1.1148 ± 0.0054	3.397 ± 0.027

TABLE 7. Concentrations of Ar (10^{-8} cm^3 STP g^{-1}) and Kr (10^{-10} cm^3 STP g^{-1}) and isotopic ratios.

				^{78}Kr/^{84}Kr	^{80}Kr/^{84}Kr	^{82}Kr/^{84}Kr	^{83}Kr/^{84}Kr	^{86}Kr/^{84}Kr
^{36}Ar	^{36}Ar/^{38}Ar	^{40}Ar/^{36}Ar	^{84}Kr			^{84}Kr = 100		
4.262 ± 0.037	3.627 ± 0.039	1335 ± 14	0.354 ± 0.031	1.83 ± 0.83	60.2 ± 5.1	49.9 ± 5.1	32.5 ± 3.6	34.1 ± 3.8

TABLE 8. Xenon concentration (10^{-10} cm^3 STP g^{-1}) and isotopic ratios.

	^{124}Xe/^{132}Xe	^{126}Xe/^{132}Xe	^{128}Xe/^{132}Xe	^{129}Xe/^{132}Xe	^{130}Xe/^{132}Xe	^{131}Xe/^{132}Xe	^{134}Xe/^{132}Xe	^{136}Xe/^{132}Xe
^{132}Xe				^{132}Xe = 100				
0.041 ± 0.013	5.0 ± 1.5	11.7 ± 3.0	29.2 ± 8.6	207 ± 55	29 ± 12	96 ± 48	60 ± 26	n.d.

Supporting information. Bulk densities (volume including internal voids) as well as grain densities (volume of solids only) were determined.

The bulk volumes and densities of the individual meteorites F05 (21.08 g) and F06 (14.15 g) were obtained using structured-light optical scanning as

TABLE 9. Cosmogenic isotope concentrations (10^{-8} cm^3 STP g^{-1}), shielding conditions (preatmospheric meteoroid radius and sample depth within the meteoroid), production rates P_x (in 10^{-8} cm^3/[g×Ma]), and cosmic ray exposure ages T_x (Ma). T_x ranges determined based on minimum and maximum cosmogenic isotope concentrations and production rates.

^{3}He$_{cos}$	^{21}Ne$_{cos}$	^{38}Ar$_{cos}$	Radius (cm)[a]	Depth (cm)	P_3	P_{21}	P_{38}	T_3	T_{21}	T_{38}
92.89 ± 0.38	27.34 ± 0.22	0.421 ± 0.016	20–30	8–14	2.00–2.11	0.44–0.50	0.024–0.027	44–47	55–62	15–18

[a]See text for constraints on maximum radius.

TABLE 10. Radiogenic isotope concentrations (10^{-8} cm^3 STP g^{-1}), K concentrations (ppm), U and Th concentrations (ppb), and U/Th-He and K-Ar gas retention ages T_x (Ga).

^{4}He$_{rad}$	^{40}Ar$_{rad}$	K[a]	U[a]	Th[a]	T_4	T_{40}
908 ± 42	5100 ± 600	1211	11	66	2.3–2.5	3.3–3.7

[a]From Table 4.

2.6093 ± 0.0010 g cm^{-3} and 2.6412 ± 0.0004 g cm^{-3}, respectively (Table 11). For the individual meteorite F07 (10.11 g), F69 (1.94 g) and F82 (1.43 g), X-ray computed micro-tomography (μXCT; compare Figure S3) provided bulk volumes and corresponding bulk densities of 2.605 ± 0.007 g cm^{-3}, 2.714 ± 0.010 g cm^{-3}, and 2.509 ± 0.010 g cm^{-3}, respectively (Table 11).

Helium pycnometry of specimen F07 provided the solid volume and a corresponding grain density of 3.1265 ± 0.0011 g cm^{-3} (Table 11). The difference between the bulk and grain densities indicates an internal porosity of 16.7 ± 0.3%. μXCT imaging suggests that this porosity is mainly present as micro-fractures between clasts and matrix and within enstatite crystals (Figure S3). He-pycnometric grain density determination of fragment AKM03B provided a value of 3.127 ± 0.005 g cm^{-3} (Table 11) in excellent agreement with the grain density of the larger individual F07.

The bulk densities of Ribbeck individuals of 2.51–2.71 g cm^{-3} are at the lower end of the range reported for aubrites, which vary between 2.53 and 3.10 g cm^{-3} (Macke et al., 2011). This can be explained by the porosity of Ribbeck, if the 16.7% found in F07 is taken as representative. This value is high compared to samples of other aubrites where porosities around 10% or lower are commonly found, with notable exceptions of 15.5% in Bishopville and 21.4% in Khor Temiki (Macke et al., 2011). The low bulk density of the small but highly oriented individual F82 likely results from a large volume fraction of frothy fusion crust. Such crust is absent on F69 and only adds a minor contribution to the bulk volume of F07.

The grain densities determined for AKM03B and F07 fall also at the low end of values reported for aubrites ranging between 3.14 and 3.29 g cm^{-3} and is most similar to values determined for samples of Khor Temiki and Pesanoye (3.14 ± 0.01 g cm^{-3}; Macke et al., 2011). Because the masses of AKM03B and F07 at 2.42 and 10.11 g, respectively, are rather small compared to the typical masses of 16–80 g used by Macke et al. (2011), the measured grain density might be biased toward low values due to the bubbly fusion crust on the rear side of the flight-oriented individual F07 or the chance absence of larger metal particles. However, assuming the presence of a 3-mm spherical Fe metal particle—replacing an equal volume of the silicate material—would increase the overall grain density by only 0.7%, suggesting that stochastic effects are negligible. Moreover, μXCT confirmed the presence of multiple metal particles in F07 up to 1.3 mm in size and accounting for about 0.1 vol% of the sample. μXCT also suggests that the fusion crust is a very minor contribution to the total volume and may be assumed negligible as well. The excellent agreement between individual F07 and the partially fusion-crusted fragment AKM03B underlines this.

A model density based on the 2D modal abundances of enstatite (3.19 g cm^{-3}), forsterite (3.27 g cm^{-3}), plagioclase (2.62 g cm^{-3}), sulfide (troilite, 4.85 g cm^{-3}), and metal (7.90 g cm^{-3}) results in 3.17 ± 0.13 g cm^{-3}, which is consistent with the measured value, although the uncertainty is high due to the uncertainty in the modal abundances. The high plagioclase abundance of ~15 vol% is likely the main reason for the low grain density. The high plagioclase mode is similar to the 16.2 vol% found in Bishopville, whereas most other aubrites exhibit plagioclase abundances below 3 vol%, with the exception of Khor Temiki at 6.6 vol% (Watters & Prinz, 1979).

Aubrites appear to be unique among all meteorite groups for their extreme heterogeneity in the abundance of ferromagnetic metal (Rochette et al., 2009). This is clearly due to the generally coarse-grained texture with metal nuggets of various sizes embedded in rather large enstatite crystals. The mean MS value of six analyzed Ribbeck stones between 21.08 and 0.87 g is log(MS) = 3.13. It is significantly below the average of the aubrite family; this goes along with a relatively moderate variability resulting in a standard deviation of 0.26 (Figure S5). The
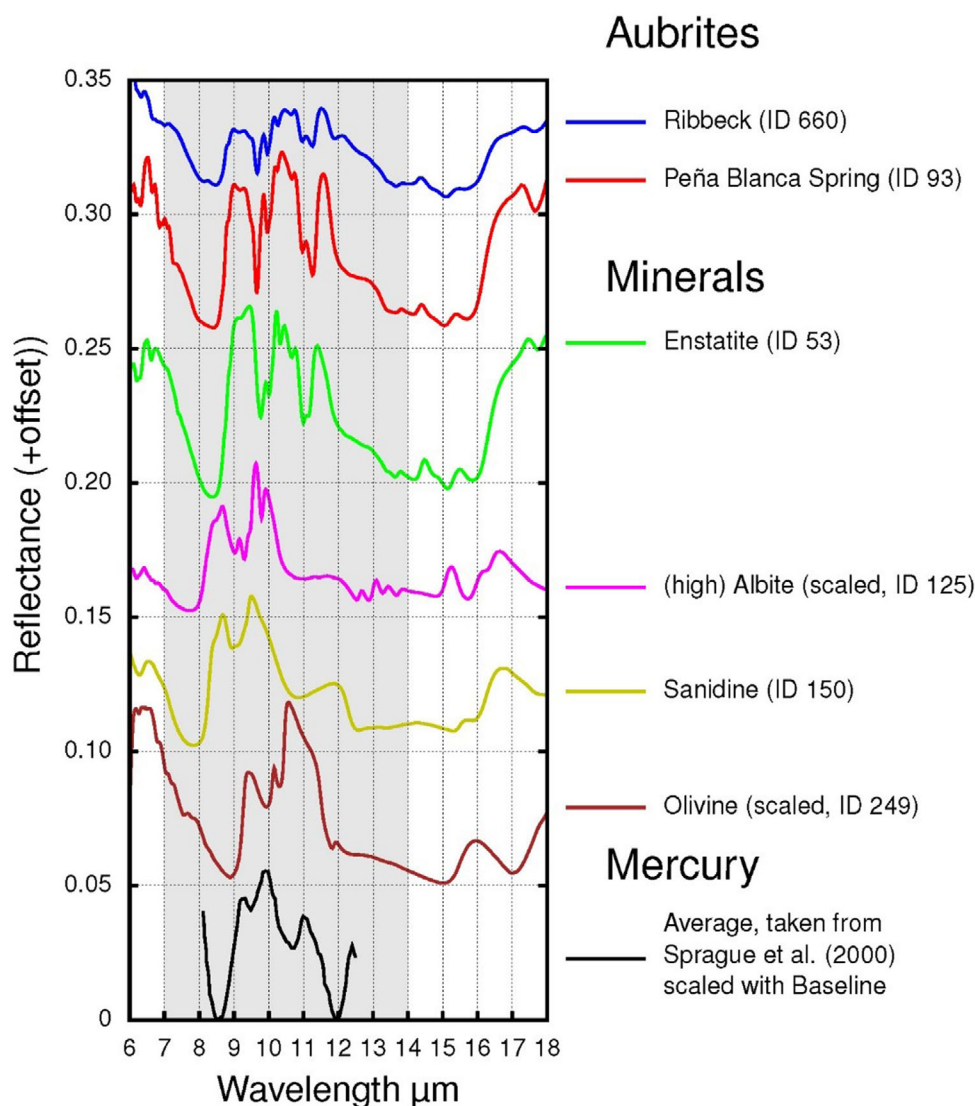
FIGURE 13. Spectra of Ribbeck powder sample (ID 660; top) and Peña Blanca Spring (ID 93, grain size 25–63 μm), compared to spectra of the pure minerals (IDs 53, 125, 150, and 249, grain size 25–63 μm) of which the Ribbeck meteorite are comprised. All spectra are measured with the same viewing geometry with an angle of incidence and emergence of 30° and are taken from the MERTIS IRIS Infrared database, under which they can be found with their IDs. The Mercury average spectrum at the bottom is an emission spectrum turned into reflectance using Kirchhoff's law (Nicodemus, 1965). The gray region between 7 and 14 μm indicates the measurement range of the MERTIS instrument (Hiesinger et al., 2020).

TABLE 11. Density measurements on different fragments of Ribbeck.

Sample	Mass (g)	Volume (cm^3)	Density (g cm^{-3})	Density type	Method
AKM03B	2.4178 (4)	0.7733 (11)	3.127 (5)	Grain	He pycnometry
F05	21.08 (1)	8.0788 (2)	2.6093 (10)	Bulk	Optical scanning
F06	14.154 (2)	5.3590 (2)	2.6412 (4)	Bulk	Optical scanning
F07	10.1132 (4)	3.882 (11)	2.605 (7)	Bulk	μXCT
F07	10.1132 (4)	3.2347 (11)	3.1265 (11)	Grain	He pycnometry
F69	1.937 (1)	0.7136 (20)	2.714 (10)	Bulk	μXCT
F82	1.426 (1)	0.5683 (20)	2.509 (10)	Bulk	μXCT

TABLE 12. Specific activities of radionuclides determined by gamma spectrometry.

Radionuclide	Half-life	Specific activity (dpm kg^{-1}), Flensburg	σ (%)	Specific activity (dpm kg^{-1}), Ribbeck (AKM01)	σ (%)	Specific activity (dpm kg^{-1}), Ribbeck (AKM05)	σ (%)
Cosmogenic							
^{7}Be	53.22 d	121	14	147	10	117	16
^{22}Na	2.6029 yr	65	8.8	90	7.5	92	14
^{26}Al	7.05 10^5 yr	<1.7		73	7.4	58	13
^{46}Sc	83.787 d	12.6	13	<3.0		<2.7	
^{44}Ti	60.0 yr	n.a.		<2.2		<1.1	
^{48}V	15.9735 d	26	17	<5.7		<6.2	
^{51}Cr	27.704 d	116	21	<37		<37	
^{52}Mn	5.592 d	n.a.		<30		<29	
^{54}Mn	312.19 d	150	8.0	4.8	17	5.6	20
^{56}Co	77.236 d	7.3	19	<3.0		<2.7	
^{57}Co	271.81 d	13.5	13	<2.0		<1.5	
^{58}Co	70.85 d	16.4	13	<2.5		<2.6	
^{60}Co	5.2711 yr	98	8.1	<2.8		<2.3	
Primordial and decay series							
^{238}U decay series:							
^{238}U	4.468 10^9 yr	<22		<60		<38	
^{226}Ra	1600 yr	13.3	11	8.1	19	<11	
^{210}Pb	22.23 yr	< 27		<110		<56	
^{232}Th decay series:							
^{228}Ra	5.75 yr	<24	15	31	13	<16	
^{228}Th	1.9126 yr	16.6	13	30.6	6.9	11.2	22
^{40}K	1.2504 10^9 yr	780	8.1	3000	8.0	2200	14

Note: All activity data are referenced to the date of the respective falls, i.e., September 12, 2019 (Flensburg), and January 21, 2024 (Ribbeck; stones AKM01 and AKM05; Table S1). Half-lives are from the Decay Data Evaluation Project (DDEP, 2023) or for ^{26}Al from Norris et al. (1983). Data about the German fall Flensburg (Bischoff et al., 2021) are included for comparison to demonstrate the remarkable differences between the nuclide activities in chondritic and achondritic rocks. Nearly all heavier radionuclides are missing in Ribbeck due to the low target element Fe, Ni, (and Co) concentrations.

Abbreviation: n.a., not analyzed.

TABLE 13. Nuclide ratios measured by IAMS and resulting specific radionuclide activities in Ribbeck.

	^{26}Al/^{27}Al	^{26}Al (dpm kg^{-1})	^{41}Ca/^{40}Ca	^{41}Ca (dpm kg^{-1})
Ribbeck	$(1.314 \pm 0.064) \times 10^{-10}$	66.9 ± 3.3	$(3.6 \pm 1.2) \times 10^{-13}$	0.80 ± 0.27
Blank	$(2.6 \pm 1.5) \times 10^{-15}$		$<3 \times 10^{-15}$	

Note: Total uncertainties include also those from the standards.

corresponding content of ferromagnetic metal of the measured individuals varies within a range of about 0.1–0.6 wt%.

Short- and Long-Lived Radionuclides by Gamma Spectrometry

For Ribbeck samples AKM01 (recovered 6 days after the fall event; start of analysis: January, 29) and AKM05 (found 8 days after the fall; start of analysis: January, 31), the gamma lines from members of the natural decay series of the primordial nuclides ^{238}U and ^{232}Th as well as of ^{40}K (Table 12) and short-lived cosmogenic nuclides were detected. A total number of four cosmogenic radionuclides were detected above the decision thresholds of the method. Their half-lives range from 53 days (^{7}Be; DDEP, 2023) up to 705,000 years (^{26}Al; Norris et al., 1983). Heavier radionuclides—^{44}Ti to ^{60}Co, which are typically identified in chondrite falls—are absent due to the low concentrations of heavy target elements, i.e. mainly iron and nickel (and Co for ^{60}Co). Solely short-lived ^{54}Mn could be positively detected in Ribbeck, but 31 times lower than in Flensburg, which is roughly the same factor as the bulk iron value in Ribbeck relative to Flensburg (27×).

The radionuclide data (Table 12) do not allow any statement about possible disequilibria in the decay series. However, assuming an equilibrium state of the decay series, the terrestrial isotope ratios, and a homogenous
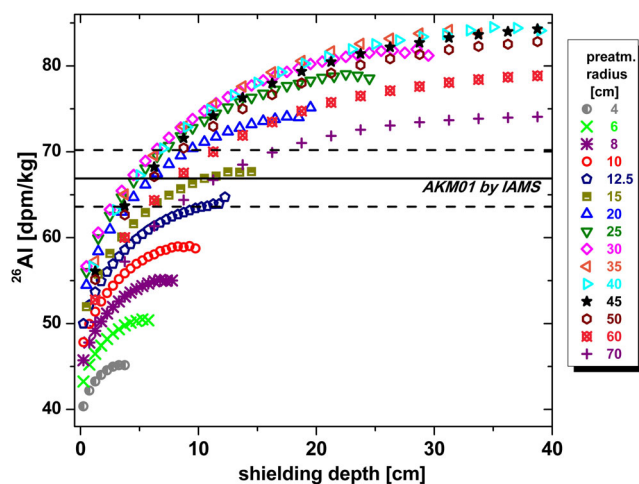
FIGURE 14. ^{26}Al specific activity of Ribbeck (black line) calculated from IAMS data with 1-sigma uncertainties (black dotted lines) compared to radius- and depth-dependent (saturation) production rate calculations for ^{26}Al for ordinary chondrites (Leya et al., 2021). The production rates are based on the chemical composition in Table 4.

distribution in each sample, the U, Th and K concentrations of the sample AKM01 would be 10.9 ± 2.0 ng g^{-1}, 126 ± 8 ng g^{-1} and 1620 ± 130 µg g^{-1}, respectively. For sample AKM05, we calculated Th and K concentrations of 46 ± 10 ng g^{-1} and 1200 ± 160 µg g^{-1}, respectively. Uranium was below the detection limit of 15 ng g^{-1}. The values of both samples differ from each other and from the bulk data in Table 5, indicating the heterogeneity of the entire body.

Constraints on Preatmospheric Radius and Shielding Depths by Cosmogenic Radionuclides

The instrumental accelerator mass spectrometry (IAMS) determined nuclide ratios that can be explained by a long CRE age (resulting in saturation of the respective radionuclide), i.e., about 10^{-10} and 10^{-13} for ^{26}Al/^{27}Al and ^{41}Ca/^{40}Ca, respectively (Table 13). Associated machine blanks were two to five orders of magnitude lower, so no blank correction was applied to the results. No further uncertainty was added to the specific activities for stable Al and Ca concentration values. As the IAMS samples (containing only about 1% Al and Ca each, Table 4) generally result in lower stable nuclide currents than those from chemically processed Al$_2$O$_3$ and CaF$_2$ samples ($\sim$2.5%), the counting statistics show low results. The ^{41}Ca concentration is equally low as the other heavy radionuclides (Table 12) due to missing heavy target elements.

The ^{26}Al value from IAMS (originating from a 0.75 g aliquot of AKM01) is in excellent agreement with the ^{26}Al values from gamma spectrometry (originating from AKM01 and AKM05; Figure S6). The comparison (Figure 14) of the IAMS experimental ^{26}Al with radius- and depth-dependent (saturation) production rate calculations, developed for L chondrites (Leya et al., 2021), let us exclude preatmospheric radii of up to 10 cm. This clearly confirms previous calculations suggesting a radius of about 22 cm (Spurný et al., 2024) and the noble gas results (this work). Considering a radius of 20–25 cm, the powdered AKM01 sample was exposed to cosmic rays at a rather shallow depth between 3 and 10 cm only (but see also noble gas discussion suggesting slightly larger depth and pre-atmospheric radius). The gamma spectrometry results of ^{26}Al for AKM01 and AKM05 are compatible with the IAMS result interpretation.

The experimental ^{41}Ca/^{40}Ca of Ribbeck is, as expected, an order of magnitude lower than that of ordinary chondrites ($\sim 10^{-12}$; Bischoff et al., 2024), since the main target element for ^{41}Ca production, iron (Table 4), producing around two-thirds of all ^{41}Ca, is more than an order of magnitude less abundant in aubrites. As the stable Ca concentration of Ribbeck is comparable to that of ordinary chondrites, the specific activity of ^{41}Ca is also more than an order of magnitude lower than that of ordinary chondrites. However, for ^{41}Ca we can only compare our experimental data with calculations by Leya and Masarik (2009) developed for ordinary chondrites. These calculated production rates—based on the bulk composition of Ribbeck, i.e., 0.78% Fe—do not reach values higher than 0.36 dpm kg^{-1} under any shielding geometry, which is incompatible with the measured (0.80 ± 0.27) dpm kg^{-1}. We will need a bulk iron concentration of $\sim$2.5% to obtain calculated ^{41}Ca values in the range of the experimental one for radii of 20–25 cm. Thus, if we exclude the possibility of incorrect experimental data for ^{41}Ca (IAMS) and Fe (Table 4), we should probably question whether the use of Monte Carlo-calculated production rates for ordinary chondrites is applicable to aubrites. However, as pointed out earlier (Bischoff et al., 2024), there is a need for updated ^{41}Ca production rate calculations, even for ordinary chondrites.

The gamma-measured specific activities of ^{22}Na for Ribbeck (AKM01 and AKM05) compared to radius- and depth-dependent (saturation) production rate calculations for ^{22}Na (Leya et al., 2021; Figure S7) can only be explained by a preatmospheric rather near-surface exposure within a body of smaller radii (<12.5 cm). It must be noted that the ^{22}Na is much higher for an aubrite chemical composition than for an ordinary chondrite (Bischoff et al., 2024), as the radionuclide is mainly produced from Mg and only to a lesser extent from Si and Na in such shielding conditions. It is questionable, if production rates calculated for an ordinary chondritic matrix are applicable to aubrites, as such small

preatmospheric radii is unlikely and not compatible with the meteoroid's atmospheric trajectory and the strewn field calculations, [26]Al and noble gas results.

DISCUSSION

Classification of Ribbeck

Based on the modal mineralogy and the mineral chemistry, Ribbeck must be classified as an aubrite. It mainly consists of coarse-grained, millimeter- to centimeter-sized crystals of enstatite. The minor abundant plagioclase and olivine crystals can also reach sizes in the millimeter range. In addition, small abundances (<1 vol%) of Ca-pyroxene and K-feldspar are present. The occurrence of troilite, djerfisherite, alabandite, oldhamite and minor kamacite, taenite and schreibersite is typical for aubrites. All silicates are highly reduced and basically free of Fe. The low bulk concentration of Fe (<1 wt%) is due to the occurrence of sulfides and minor metals and schreibersite. Ribbeck is severely brecciated, but does not contain solar wind implanted gases. Thus, the rock is a fragmental breccia.

The chemical composition is very similar to that of the aubrite Bishopville. Bishopville is a feldspar-bearing aubrite, and the relatively high concentration of Al (1.22 wt%) in Ribbeck points toward a remarkable abundance of feldspar, which is confirmed by the finding of abundant albitic plagioclase and minor K-feldspar. Thus, based on the bulk chemistry and the mineralogy, Ribbeck plots close to the REE-poor (Figure 11) and feldspar-rich end of the aubrite field, while the aubrite Norton County marks the opposite boundary. The O-isotope compositions of two small chips and the Ti-isotopes from the 4.3 g specimen of Ribbeck are indistinguishable from other aubrites (Figures 10 and 12). Both the O and Ti isotopes are similar to values for the BSE and E chondrites. For O, the isotopically closest aubrite is Elephant Moraine 90033 (The Meteoritical Bulletin, 2024).

Considering the bulk composition of aubrites, Ribbeck has low abundance of REE with a strong positive Eu anomaly, very similar to that of Bishopville (Figure 11). Eu-anomalies strongly suggest that igneous processes have been at work as already mentioned by Okada et al. (1988). In Ribbeck large plagioclase crystals were encountered (Figure 5c) indicating crystal growth in a slowly cooled environment. The texture of plagioclase fragments clearly shows that the plagioclase fragments derive from a coarse-grained magmatic lithology that had been fragmented by impact and not from a shattered volcanic rock.

Considering all data we currently have, Ribbeck is a fragmental breccia, mineralogically similar to Bishopville.

The modal abundances of enstatite, plagioclase, and sulfides are remarkably similar to those determined for Bishopville by Wilbur et al. (2022). Ribbeck is shocked to S3 (U-S3), and it clearly shows the initial effects of terrestrial weathering (at least W0/1) after being in a wet environment for 6 days before recovery. After the formation of the breccia by re-accretion, the melt veins and melt areas (Figure 8e,f) formed within the fine-grained clastic areas indicate at least one additional late impact event. Thus, Ribbeck experienced a complex impact-related history. Similar observations were reported from Bishopville (Wilbur et al., 2022).

Interpretation of the FT-IR Spectroscopy Data and the Relationship to Mercury Rocks and the BepiColombo Mission

The ESA/JAXA joint mission BepiColombo is dedicated to exploring Mercury, the innermost solar system planet. The spacecraft has a mid-infrared spectrometer (MERTIS—Mercury Radiometer and Thermal Infrared Spectrometer) on board to map the surface of Mercury (e.g., Benkhoff et al., 2010; Helbert et al., 2007; Hiesinger et al., 2010; Morlok et al., 2020). Since meteorite samples definitely associated with Mercury are not available in our meteorite collections, other types of achondritic meteorites are suggested as analog materials for Mercury's surface rocks. Generally, aubrites (e.g., Keil, 2010; Love & Keil, 1995; Udry et al., 2019) or related materials (e.g., NWA 7325; e.g., Irving et al., 2013; Weber et al., 2016) have been considered good candidates. We thus discuss in-depth the analysis of the fresh aubrite Ribbeck by IR spectroscopy in the following.

In the past, components of aubrites have been studied by mid-infrared spectroscopy. Morlok et al. (2020) showed that comparing aubrites with a large-scale surface spectrum of Mercury does not provide a suitable fit. Only spectra from a quenched impact melt lithology show similarity; these spectra were obtained from melt veins of Norton County, characterized by a dominating strong RB between 10.8 and 11.1 μm (Morlok et al., 2020). However, this type of lithology is quite unusual and rare in aubrites.

The spectrum of the powder sample from Ribbeck analyzed here contains 16 well-resolved peaks and two clearly visible underlying peaks visible as shoulders of larger peaks in the mid-infrared wavelength range between 6 and 18 μm (Figure 13).

Comparing the Ribbeck sample spectrum (ID 660) and the spectrum of the aubrite Peña Blanca Spring (PBS, ID 93, grain size of shown spectrum 25–63 μm) shows an overall concordance (Morlok et al., 2020; Figure 13). This demonstrates the mineralogic homogeneity of the aubrites, which are all rich in iron-poor pyroxene. This is also documented by the similarity of the pure mineral spectrum

of enstatite (ID 53) with the spectra of Ribbeck and PBS (Figure 13) and the MIR data of Cantillo et al. (2024) from Ribbeck.

Cantillo et al. (2024) find a similar spectral behavior to our spectra in their measured MIR range up to 14.2 μm, which they generally intereprted as iron-poor enstatite. However, the wavelength of PBS's CF is at 8.3 μm (Morlok et al., 2020), whereas Ribbeck's CF has a doublet-like occurrence with two minima at 8.15 and 8.49 μm, divided by a weak peak at 8.25 μm. This feature seems also to be visible in Cantillo et al. (2024) but was overseen or not discussed although they reported the CF at 8.1 μm. This occurrence of the CF is due to the plagioclase, with its high Ab content. Pure (or high contents of) albite has a strong band between its CF at 7.74 and 9.01 μm (Reitze et al., 2021). This strong plagioclase feature is responsible for the shape of the CF region on the Ribbeck spectrum.

Interestingly, the best resolved doublet CF in Cantillo et al. (2024) is in their finest grain size fraction below 45 μm. This is in accordance with Taylor et al. (2001) and Reitze et al. (2021). Taylor et al. (2001) found that plagioclase is enriched in the finest fraction of the lunar regolith after seving regolith samples. Spectroscopically, the same behavior was observed by Reitze et al. (2021) who find that the plagiclase component is enriched in the finer-grained fractions and, therefore, better visible in the MIR spectra of their samples.

Further, also low-Ab plagioclase has a strong band in this wavelength range. High and low plagioclase differ in their degree of Al,Si order and in their respective spectra, which is a function of the equilibration temperature (e.g., Kroll, 1973; Reitze et al., 2020). Therefore, the spectral shape might also help to identify the equilibration temperature of the meteorite. In turn, knowing the (exact) spectral (plagioclase) endmember would help to identify the parent body of the aubrites via remote sensing. In addition, the detected K-feldspar component in Ribbeck (see above), which is suggested to be sanidine, might also have a proportion, although its amount is comparatively low in Ribbeck. A similar observation was reported by Weber et al. (2023), who indicated that plagioclase RBs were not directly visible in synthetic mineral mixtures with high pyroxene contents. However, a clear influence on the CF was detectable. The olivine content of Ribbeck is visible by the weak peak at ~12 μm characteristic of olivine (e.g., Weber et al., 2021). The strong feature around 11.5 μm, which is highly affected by the enstatite content, might mask the spectral signature of alteration phases of oldhamite, like aragonite (e.g., Reitze et al., 2024). The sulfite (SO_3) complex would have a strong band at around 10.58 μm, and the sulfate (SO_4) complex would appear at around 9.10 μm (e.g., Tseng, 1984); the SO_3 complex is an especially expected alteration component of oldhamite (Reitze et al., 2024). However, no clear peaks associated with sulfite or sulfate are detectable in Ribbeck's spectrum. Therefore, if S is present in SO_3 or SO_4 complexes, especially in alteration phases of sulfides, the modal abundance is so low that it is not visible in Ribbeck's bulk sample spectrum. We also cannot rule out that significant parts of S were lost from the Ribbeck stones by degassing of H_2S as reported above.

As stated above, aubrites are especially debated as analog materials of Mercury because of their element abundances, ratios, reduced mineralogy, and depletion of volatile elements, which are suggested to be similar in both the aubrite parent body and Mercury, which implies similar geochemical building regimes within both bodies (e.g., Steenstra & van Westrenen, 2020). Therefore, the mineral phases and their mixtures present in the aubrites and their respective spectra are important for the MERTIS on board BepiColombo, which will investigate the hermean surface in the mid-infrared range (Hiesinger et al., 2020). Yet, comparing an average emission spectrum of Mercury taken from Sprague et al. (2000), converted into reflectance, with the Ribbeck meteorite spectrum does not show any meaningful similarities (Figure 13). This general observation supports earlier conclusions concerning studies on aubrite constituents (Morlok et al., 2020). In fact, the Mercury average spectrum was interpreted as being dominated by ultramafic basalt with high MgO contents (Sprague et al., 2000).

Yet, the surface of Mercury might have some similarities to the Ribbeck meteorite. The Mercury spectrum displays an average of a large area of the hermean surface, which "averages out" small scale variations of the chemical and, therefore, mineralogic composition. In addition, the comparatively high plagioclase content of the Ribbeck meteorite makes it more similar to Mercury surface components, since plagioclase is expected to be a major surface constituent (e.g., Namur & Charlier, 2016). Therefore, small outcrops on Mercury's surface may show other mineralogical compositions, more similar to those of aubrites. A potential region incorporating a similar composition might be the hollows on Mercury, in which sulfides like oldhamite are expected (e.g., Renggli et al., 2022). Therefore, the spectrum of the Ribbeck meteorite can help to understand the remote sensing spectra of Mercury and can help to test hypotheses on the mineral mixture of the hermean surface.

However, when considering the relationship between aubrites and Mercury surface components, one must account for the effects of space weathering. As e.g., summarized by Markus et al. (2024), the products of space weathering are generally a function of the location within the solar system, the type of surface, the length of time a surface has been exposed to the space environmental
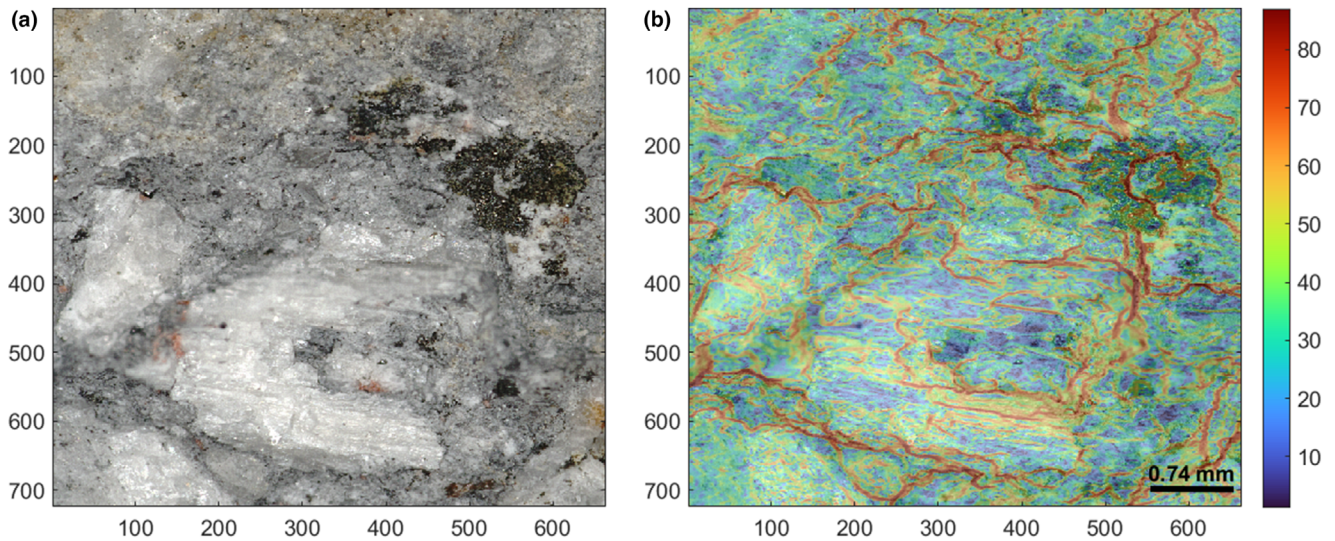
FIGURE 15. (a) Optical image of the analyzed region of interest. Visible enstatite crystals (bright) and sulfides (black) are embedded into a fine-grained matrix of rock debris (light gray). (b) Slope map of the same region of interest as shown in (a). Note the parallel slopes indicating the cleavage planes of the large enstatite grain. Axis are pixel, where 1 pixel = 7 μm.

conditions and the present mineralogical composition. In general, nanophase iron (npFe^0) inclusions have been documented as a very typical space weathering product, which is well known and has been studied in detail considering lunar regolith samples and soils (e.g., Keller & McKay, 1993, 1997; Pieters & Noble, 2016).

On all parent bodies micrometeorite bombardment and solar wind irradiation result in the formation of npFe^0, which is a well-studied and well-considered phenomenon (e.g., Brunetto et al., 2014; Brunetto & Strazzulla, 2005; Zhang et al., 2022). Markus et al. (2024) also state that ion irradiation also leads to npFe^0 directly on the surface of irradiated silicates or through redeposition of sputtered deposits (see also Stojic et al., 2023 for sputter and melt redeposition). On the Moon, the npFe^0 formation is easy to consider, since the lunar rocks contain Fe-bearing minerals (olivine and pyroxene with variable FeO-concentrations). Lunar-like space-weathering may play only a minor role on Mercury having basically FeO-poor silicates (compare Loeffler et al., 2016). Instead, the low abundance of Fe,Ni metals and Fe-bearing metals within the precursor rocks of Mercury could lead to impact-related modifications. These may include grain size reduction of opaque phases and processes of shock darkening based on impact vaporization of Fe-rich components and redeposition on silicate fractures and spaces. Darkening of surface lithologies may also be related to reduction of mineral grain sizes by large-scale impact processes as well as by micrometeorite impacts.

With growing interest in characterizing the physical properties of boulders on planetary surfaces using modeling techniques, remote sensing, and laboratory experiments (e.g. Grott et al., 2019; Molaro et al., 2020; Patzek et al., 2024; Patzek & Rüsch, 2022; Sun & Lucey, 2023; Tatsumi et al., 2021), the surface roughness of rocks is naturally of interest because of its influence on reflection (photometry) and thermal radiation. Despite the known caveats in using meteorites and their unpolished surfaces as analogues to surfaces of freshly exposed boulders on airless planetary bodies, concerning their exposure history and physical properties, we provide for Ribbeck the surface average slope and Hapke mean slope angle at the ~7 μm scale to be ~38° and 32°, respectively. These values of the surface average slope and mean Hapke slope are generally in the range of values derived, at the ~4 μm resolution, for a suite of different meteorites belonging to different groups (Marshal et al., 2024), further indicating that petrology has little effect on these mean values. Worth noting is the rather uncommon spatial pattern of slopes observed for the sample with characteristic parallel high slope lineations associated with the cleavage plane of single (large) crystals (enstatite) (Figure 15b).

Could Altered Phases Observed in Ribbeck Partly be of Extraterrestrial Origin?

It is well known that oldhamite reacts very fast in wet environments in order to form secondary terrestrial alteration products, as also reported after the Neuschwanstein E chondrite meteorite fall (e.g., Zipfel et al., 2010). In a similar manner, the oldhamites in Ribbeck are already in the process of weathering, as

indicated by textural features (Figure 9); however, the strong degree of alteration even after only 6 days in the wet environment is very surprising. In the case of the E chondrite Neuschwanstein, the degree of alteration of oldhamite was much less pronounced, although the first specimen was found more than 3 months after the fall. In both cases (Ribbeck and Neuschwanstein), the conditions were similar: The specimens impacted into snow that melted afterward (albeit within a few days vs. several months). The question is whether terrestrial weathering is the only process responsible for the extreme degree of alteration of oldhamite in Ribbeck (Figure 9c,d).

Two other phases are also heavily altered (Figure 7), resulting in low analytical totals of about 80 wt% (Table 2). Yet, as stated above, we observed no reaction zones around the grains nor veins filled with secondary alteration products within neighboring minerals (Figure 7a,d). One of these phases is rich in Cr ($\sim$31 wt%) and S ($\sim$41 wt%; Table 2). Based on the high Cr concentration, we suggest that the original phase was caswellsilverite or a Ca-bearing similar sulfide that could immediately be transformed into the altered Cr-rich, probably water-bearing phase (or mixtures of alteration products; Table 2; Figure 7). The most surprising aspect is again the degree of alteration. The grains must have been completely transformed into this (these) new secondary alteration phase (or phases) within 6 days. Because of the very low Fe-concentration (0.5 wt%; Table 2) the precursor phase is probably not daubréelite, which is still stable in other aubrites and E chondrites even many years after their fall events. The Ca-bearing Cr-rich alteration product could be similar to cronusite ($Ca_{0.2}CrS_2 \times H_2O$) and/or related to a Na-poor version of schöllhornite ($Na_{0.3}CrS_2 \times H_2O$). It is possible that the Ca-concentration of about 5 wt% (Table 2) results from weathering of oldhamite and could have filled vacancies in the schollhornite structure and/or has replaced the Na cations in the structure. A similar alteration process is suggested for the Ti-rich phase (Table 2) that could be an alteration product of heideite or a different precursor (parental) phase yet-to-be-identified.

Based on the strong degree of alteration and of the lack of reaction features in the immediate surroundings or in the vicinity the three phases discussed above, we cannot completely rule out that the alteration partly happened before the meteorite atmospheric entry, and that some grains (especially the Cr-rich grains) may represent extraterrestrial phases (perhaps sulfates). As discussed in detail, Ribbeck is a highly brecciated rock. The only way to explain the occurrence of these "water-rich" phases or "sulfates" in a rock composed of highly reduced components would be that these phases were originally part of a regolith component, perhaps entered the regolith

as projectiles. However, this speculation goes too far and this scenario will not be discussed in more detail.

The Brecciated Nature of Aubrites like Ribbeck

Ribbeck was brecciated on its parent body(ies). As shown in many images (Figures 2 and 5 and Figure S1) millimeter- to centimeter-sized clasts (typically enstatite rich) are embedded in a fine-grained clastic matrix consisting of debris from the major meteorite components. It is uncertain whether all the components formed on one aubrite parent body or whether the different components are related to mixing of components from different geochemically/isotopically indistinguishable aubritic parent bodies after destructive collision and reassembly. The latter case is certainly possible considering the large fragment with a radial pyroxene-like texture. This type of texture is normally found in chondrules. However, we emphasize that in this case there is no reasonable argument for having a chondritic component.

As summarized by Bischoff et al. (2006), meteoritic breccias are known to have formed on a variety of parent bodies (Burbine et al., 2002). Often, a large fraction of samples of a specific meteorite group are brecciated. This is the case, for example, for CI and CM chondrites, mesosiderites, aubrites, and HED meteorites (e.g., Alfing et al., 2019; Bischoff et al., 2006; Keil, 1982, 2010; Lentfort et al., 2021). Only four groups of stony meteorites appear to lack clearly defined breccias: angrites, brachinites, acapulcoites and lodranites, as pointed out by Bischoff et al. (2006).

Brecciated meteorites like Ribbeck provide important information about the history and evolution of the asteroids and impact processes on small bodies (Keil, 1982), certainly much more than unbrecciated meteorites do. The most extreme cases are the polymict breccias of Kaidun and Almahata Sitta (e.g., Bischoff et al., 2010; Bischoff, Bannemann, et al., 2022; Horstmann & Bischoff, 2014; Zolensky et al., 2010; Zolensky & Ivanov, 2003). The processes that lead to the brecciated rocks we study today can be extremely and excitingly complex. These may include the formation of the primary parent body lithologies, impact-related excavation of different parent body lithologies, impact-related heating, reduction processes, metamorphism, melting, mixing and subsequent re-accretion and lithification (e.g., Bischoff et al., 2006, 2018; Keil, 1982; Keil et al., 1994, 1997; Rubin et al., 1981; Rubin, Rehfeldt, et al., 1983; Rubin, Scott, et al., 1983; Rubin & Turrin, 2023). Breccia formation like that of the Ribbeck meteorite typically requires mass transport and, therefore, the relative movement of rock fragments and their displacement from the primary location in the source material (Stöffler et al., 1988), even if this displacement can be very minor, as in

the case of monomict breccias. A subsequent impact after brecciation is required to lithify all types of breccias (e.g., Bischoff et al., 1983; Kieffer, 1975).

Considering the brecciated achondrites alone, one of the best-studied meteorites is the Norton County aubrite. Norton County is largely composed of enstatite crystals derived from ortho-pyroxenite plus pyroxenite clasts with igneous textures composed of orthoenstatite, pigeonite, diopside and impact melt breccia clasts (Okada et al., 1988). It is a fragmental breccia and, thus, lacks solar wind gases. Norton County also contains a clast composed of diopside, plagioclase, and silica, and it contains olivine grains and feldspathic clasts that are probably derived from separate lithologies. As also summarized in Bischoff et al. (2006) Norton County contains ~1.5 vol% Fe,Ni metal grains up to a centimeter in size with associated sulfides and schreibersite, which probably represent metals that were incompletely separated from silicate during differentiation (Casanova et al., 1993). Based on Okada et al. (1988), taenite compositions suggest that most metal grains cooled through 500°C at ~2°C Myr^{-1}, but that some also cooled faster. This may indicate that several major impacts must have catastrophically disrupted the parent asteroid and excavated material from various and also great depths that gravitationally reassembled, which agrees with conclusions drawn by Okada et al. (1988).

Among the brecciated aubrites, many of these rocks clearly contain parent body surface components as proved by the presence of solar wind gases (e.g., Lorenzetti et al., 2003). Among the achondrite groups, diverse abundances of breccias with solar wind gases are reported. Bischoff and Schultz (2004) and Bischoff et al. (2006) mentioned that about 40% of the howardite breccias are solar gas rich but that only ~30% of the aubrites contain solar gases, even though they are brecciated in most cases. Keil (2010) reported even fewer solar wind-containing aubrites (six of 27 aubrites studied): Bustee, Elephant Moraine (EET) 90033, Khor Temiki, Lewis Cliff (LEW) 87007, Pesyanoe, and Yamato (Y) 793592.

Bischoff et al. (2006) mentioned that other aubrites including Cumberland Falls, Bishopville and Mayo Belwa have Kr, Sm and Gd isotopic effects, indicating neutron capture near the surface of their parent asteroid for periods of up to several hundred Myr (Hidaka et al., 1999; Lorenzetti et al., 2003). Typically, aubrites with solar wind gases are composed of millimeter- to centimeter-sized clasts in a finer-grained matrix (Poupeau et al., 1974). However, for completeness it should be mentioned that other aubrites appear to be even coarser grained, with enstatite crystal fragments up to 10 cm in size (Keil, 2010; Lonsdale, 1947). Considering the statement of Poupeau et al. (1974), solar wind gases could be expected in Ribbeck, but the analysis revealed that this is not the case.

The Fragmentation of the Meteoroid and the Cumulative Mass-Number Distribution of the Recovered Fragments

The locations of the recovered fragments of Ribbeck are shown in Figure 2, and their masses are listed in Table S1. The cumulative mass-number distribution of the recovered individual Ribbeck meteorites closely follows a power law of the form $N(\geq m) \propto m^{-\beta}$ from the largest samples down to about 2.5 g. Here, $N(\geq m)$ is the cumulative number of meteorites larger than mass m. Below 2.5 g, the power law relationship (linear in log–log space) levels off. The power law behavior down to relatively small masses reflects a very effective recovery of the samples by the many search parties and their intense time commitments (>50 days by some). The power law exponent β is 1.07 ± 0.01, which is steep compared to other meteorite falls within the mass region between 2.5 and 30 g (Figure 16). Overall, Ribbeck much better resembles a power law fragmentation than most other documented meteorite falls. Together with the absence of large masses offset from the power law distribution, this suggests a thorough disruption cascade during the terminal flight phase.

The Orbit of 2024 BX1—Ribbeck

The orbit of the precursor of the Ribbeck meteorite has been determined both from observations of the meteoroid 2024 BX1 when it was still in space (Minor Planet Center, 2024a) and from observations of the bolide passing through Earth's atmosphere (Spurný et al., 2024). The semimajor axis of the orbit is 1.336 astronomical units (AU), and the eccentricity is 0.375, resulting in a perihelion distance of 0.835 AU and an aphelion distance of 1.838 AU (Minor Planet Center, 2024b).

The approach of 2024 BX1 to the Earth that resulted in the fall of the Ribbeck meteorite on January 21, 2024, occurred at the ascending node of the orbit. The descending node is close to the orbit of Mars, with a calculated minimum orbit intersection distance (MOID) of 0.048 AU. This has resulted in repeated close encounters of 2024 BX1 with both Mars and the Earth-Moon system in the past (Farnocchia, 2024).

The aphelion distance of the orbit of 2024 BX1 lies in the innermost region of the asteroid belt, which is populated by the Hungaria group of minor planets. This group is characterized by orbits with a semimajor axis between 1.78 and 2.0 AU, low eccentricities (<0.18) and high inclinations (16–34°). Among the Hungarias, there is a distinct genetic family of minor planets. Members of this family are distinguished by their high geometric albedo (~0.3–0.4) and, where known, by their E/X-type taxonomy. This family is believed to have originated from
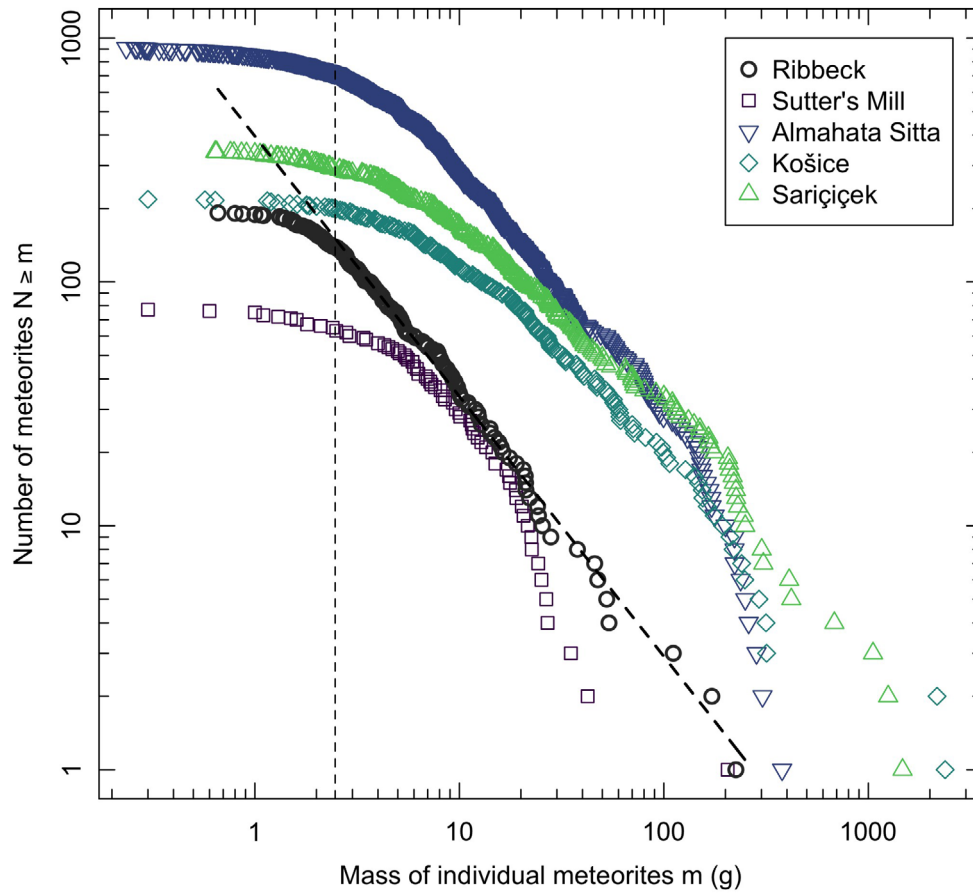
FIGURE 16. Cumulative mass-number distribution of individual Ribbeck meteorites and meteorite falls reported in the literature. The linear fit in log–log space (heavy dashed line; $R^2 = 99.3$) comprises masses from the largest recovered meteorite down to masses of 2.5 g (vertical dashed line). On extending the fit below 2.5 g, R^2 decreases due to a deficit of recovered meteorites relative to the extrapolated power law. For other meteorite falls across different types, the deviation from the power law behavior is much more pronounced (Sutter's Mill C-type chondrite, Jenniskens et al., 2012); Almahata Sitta polymict chondritic/ureilitic breccia, Shaddad et al. (2010), Bischoff, Bannemann, et al. (2022); Košice ordinary chondrite, Gritsevich et al. (2014); Sariçiçek howardite, Unsalan et al. (2019).

the catastrophic disruption of a larger asteroid ∼0.5 Gyrs ago (Warner et al., 2009), and it is considered the likely source of aubrites (Ćuk et al., 2014; Keil, 2010).

Apollo asteroids like (3103) Eger bridge the Hungaria family with the near-Earth environment (Gaffey et al., 1992). While the general size and shape of the orbits of (3103) Eger and 2024 BX1 are somewhat comparable (Table 14), the orientation of the orbits, including the inclination, is not. This rules out Eger as the direct precursor of 2024 BX1. However, a similar migration route and a common, original progenitor for both bodies might be considered. The fact that Eger retains the high inclination of Hungarias, while 2024 BX1 does not, is not a contraindication, as encounters with the Earth will decrease the inclination of the original orbit (Galiazzo et al., 2013). The cosmic ray exposure age found for Ribbeck in this study (55–62 Ma) is significantly higher

TABLE 14. Comparison of the orbital elements (Minor Planet Center, 2024c) of 2024 BX1 and (3103) Eger.

	2024 BX1	(3103) Eger
Perihelion distance $\mathbf{q}$ (AU)	0.835	0.907
Semimajor axis $\mathbf{a}$ (AU)	1.336	1.404
Aphelion distance $\mathbf{Q}$ (AU)	1.838	1.901
Eccentricity $\mathbf{e}$	0.375	0.354
Inclination $\mathbf{i}$ (°)	7.3	20.9
Long. of ascending node $\mathbf{\Omega}$ (°)	300.1	129.7
Argument of perihelion $\mathbf{\omega}$ (°)	243.7	254.1
Absolute magnitude $\mathbf{H}$ (mag)	32.7	15.3

than the typical CRE of 7–20 Ma for ordinary chondrites and HED meteorites (Eugster et al., 2006; Marti & Graf, 1992) and also higher than the CRE age of 5–30 Ma expected for meteorites ejected from Mercury (Gladman &

TABLE 15. Comparison of the orbital elements (Minor Planet Center, 2024c) of 2024 BX1 with other minor planets on similar orbits.

	2024 BX1	2012 AZ	2024 BE1	(163364) 2002 OD20	2011 BF24	2024 AZ3	(333521) 2005 PO	2010 BG5
D	–	0.018	0.029	0.037	0.039	0.039	0.045	0.047
q	0.835	0.831	0.853	0.862	0.885	0.827	0.785	0.903
a	1.336	1.338	1.327	1.365	1.385	1.269	1.252	1.472
Q	1.838	1.844	1.801	1.869	1.885	1.711	1.720	2.042
e	0.375	0.378	0.357	0.369	0.361	0.348	0.373	0.387
i	7.3	6.0	5.8	4.2	7.9	6.1	12.5	6.6
Ω	300.1	276.6	300.2	259.8	307.1	294.4	300.5	318.7
ω	243.7	264.2	241.5	275.4	244.5	246.7	249.5	216.8
H	32.7	25.8	28.9	18.9	26.2	28.8	20.1	24.0

Note: D is the D-criterion by Drummond (1981). For the other symbols, see Table 14.

Coffey, 2009). It is, however, typical for aubrites (Lorenzetti et al., 2003) and compatible with the transfer time calculated by Ćuk et al. (2014) for meteorites that originated from the inner boundary of the Hungaria region. Therefore, we consider it plausible that 2024 BX1 originated in the Hungaria family. However, further investigations of the orbit and its evolution over time seem desirable and could strengthen the connection between the 2024 BX1 and the Hungaria family.

We searched the MPCOrb database (Minor Planet Center, 2024c) for orbits similar to that of 2024 BX1. Using the D-criterion of Drummond (1981) we identified several objects on orbits that are very similar (i.e., having $D < 0.05$) to that of 2024 BX1, as listed in Table 15.

The unnumbered asteroids (2010 BG5, 2011 BF24, 2012 AZ, 2024 AZ3 and 2024 BE1) are small (assuming a geometric albedo of 0.4, their approximate diameter is between 3 and 33 m). They have been observed over a few days at most and are considered lost. Nonetheless, we highlight 2024 BE1, which was discovered by the Mt. Lemmon Sky Survey on 2024 January 19 (Minor Planet Center, 2024d) and passed 0.0055 AU from Earth on 2024 January 21 (Jet Propulsion Laboratory, 2024), about 14.5 h after the fall of the Ribbeck meteorite. Thus, both objects approached Earth at the ascending node of their orbits within a short time interval. Also, near their respective ascending nodes, the orbits of 2024 BX1 and 2024 BE1 intersect each other with a MOID calculated here of only 0.0045 AU. Therefore, the points at which the two orbits of 2024 BE1 and 2024 BX1 approached Earth and the point where both approached each other are close together. Thus, a relatively recent separation of the two objects, under the gravitational influence of the Earth, appears possible.

Considering all numbered asteroids, the orbit of (163364) 2002 OD20 is the most similar to that of 2024 BX1. However, its taxonomic class Sq (Hicks et al., 2013) seems to rule out a genetic relationship between the two. For (333521) 2005 PO, which is in 5:7 resonance with

Earth (Li et al., 2019), no information on taxonomy is available.

Ribbeck, the Third Recent Aubrite Fall and the First Achondrite among the Recent Falls in Germany

Considering all aubrite falls, Ribbeck is one of three specimens (Tiglit [2021], Rantila [2022], Ribbeck) that fell in the last 3 years (The Meteoritical Bulletin). This is very surprising, because before Tiglit, no aubrite fall was recorded for about 50 years. The last ones were Mayo Belwa (1974) and Norton County (1948) (The Meteoritical Bulletin).

Considering the recent falls in Germany it is remarkable that between the fall of Neuschwanstein (EL_a6) in April 2002 (Weyrauch et al., 2018; Zipfel et al., 2010) and Braunschweig (L6; Bartoschewitz et al., 2017) in April 2013, no meteorite had been recorded in Germany for 11 years. But starting with Braunschweig (2013), six falls occurred in the following 11 years up to today: Stubenberg (LL6; Bischoff et al., 2017; Ebert & Bischoff, 2016; Spurný et al., 2016), Renchen (L5-6; Bischoff et al., 2019a), Flensburg (C1; Bischoff et al., 2021), Elmshorn (anomalous H3-6; Bischoff et al., 2024) and Ribbeck (aubrite; this study). In the same period, the falls of Hradec Králové (LL5; 2016; The Meteoritical Bulletin), Broek in Waterland (L6, 2017; The Meteoritical Bulletin), Žd'ár nad Sázavou (L3; Spurný, 2016; Spurný et al., 2016), Ejby (H5/6; Haack et al., 2019; Spurný et al., 2017), Kindberg (L6, 2020; The Meteoritical Bulletin), and Antonin (Bischoff, Patzek et al., 2022; Shrbeny et al., 2022) were reported close by in neighboring countries. Thus, in the last 11 years, 12 meteorite falls have been recovered in an area with less than a 500 km radius (with a center near Leipzig (Germany)). Ten of these falls are ordinary chondrites; the C1 chondrite Flensburg and the Ribbeck aubrite complete this statistic.

Thus, it is remarkable that the number of recovered meteorite falls in Central Europe is surprisingly high. The

reason is (at least in part) related to the successful work of the European Fireball Network and the excellent initiatives of the American Meteor Society (AMS; https://www.amsmeteors.org/) and the International Meteor Organization (IMO; https://fma.imo.net), which motivated private search and recovery campaigns.

CONCLUSIONS

The short-lived radionuclides of the Ribbeck meteorite measured in two pieces (AKM01 and AKM05) from January 29 and January 31, 2024, respectively, for about 4 weeks confirm the connection of the Ribbeck meteorite with the bolide event near Berlin (Germany) on January 21, 2024. By June 29, 2024, an impressive 202 specimens totaling a mass of ~1.8 kg have been recovered.

All mineralogical, chemical and isotopic data show that Ribbeck undoubtedly is an aubrite. It is a fragmental breccia (Figure 5), mineralogically similar to Bishopville, and shocked to S3 (U-S3). It also shows initial effects of terrestrial weathering (W0/1) after being in a wet environment for 6 days before recovery.

The dominant mineral phase is nearly FeO-free enstatite ($En_{99.1}Fs_{<0.04}Wo_{0.9}$; 76 ± 3 vol%), but Ribbeck also contains a significant abundance (15 ± 2.5 vol%) of albitic plagioclase ($Ab_{95.3}$), which is one of the highest among all aubrites and similar to that of Bishopville, resulting in a pronounced positive Eu anomaly (Figure 11).

Oldhamite, a Cr-rich phase (perhaps altered caswellsilverite), and a Ti-rich phase show strong alteration signatures (Figures 7 and 9). Based on the strong degree of alteration and considering the lack of reaction features surrounding the three phases, it is somewhat unclear whether the alteration partially happened before the meteorite impact. Future work is needed to clarify whether specific phases (especially the Cr-rich minerals) may represent extraterrestrial phases (perhaps sulfates).

With Tiglit (2021), Rantila (2022) and Ribbeck (2024), worldwide, three aubrites fell in the last 3 years about 50 years after the last aubrite fall of Mayo Belwa (1974). Can we expect a higher fall rate of aubrites in the next few years?

Data Availability Statement—Data available on request from the authors.

Editorial Handling—Dr. A. J. Timothy Jull

REFERENCES

Alfing, J., Patzek, M., and Bischoff, A. 2019. Modal Abundances of Coarse-Grained (>5 µm) Components within CI-Chondrites and their Individual Clasts—Mixing of Various Lithologies on the CI Parent Body(Ies). *Geochemistry—Chemie der Erde* 79: 125532.

Avril, C., Malavergne, V., Caracas, R., Zanda, B., Reynard, B., Charon, E., Bobocioiu, E., et al. 2013. Raman Spectroscopic Properties and Raman Identification of CaS-MgS-MnS-FeS-Cr_2FeS_4 Sulfides in Meteorites and Reduced Sulfur-Rich Systems. *Meteoritics & Planetary Science* 48: 1415–26.

Barrat, J.-A., Zanda, B., Moynier, F., Bollinger, C., Liorzou, C., and Bayron, G. 2012. Geochemistry of CI Chondrites: Major and Trace Elements, and Cu and Zn Isotopes. *Geochimica et Cosmochimica Acta* 83: 79–92.

Barrat, J. A., Zanda, B., Jambon, A., and Bollinger, C. 2014. The Lithophile Trace Elements in Enstatite Chondrites. *Geochimica et Cosmochimica Acta* 128: 71–94.

Barrat, J.-A., Gillet, P., Dauphas, N., Bollinger, C., Etoubleau, J., Bischoff, A., and Yamaguchi, A. 2016. Evidence from Tm Anomalies for Non-CI Refractory Lithophile Element Proportions in Terrestrial Planets and Achondrites. *Geochimica et Cosmochimica Acta* 176: 1–17.

Barrat, J.-A., Greenwood, R. C., Keil, K., Rouget, M. L., Boesenberg, J. S., Zanda, B., and Franchi, I. A. 2016. The Origin of Aubrites: Evidence from Lithophile Trace Element Abundances and Oxygen Isotope Compositions. *Geochimica et Cosmochimica Acta* 192: 29–48.

Barrat, J. A., Bischoff, A., and Zanda, B. 2023. Trace Element Redistributions during Metamorphism of E-Chondrites: Implications for Reduced Bodies and the Earth. *Geochimica et Cosmochimica Acta* 356: 51–65.

Bartoschewitz, R., Appel, P., Barrat, J.-A., Bischoff, A., Caffee, M. W., Franchi, I. A., Gabelica, Z., et al. 2017. The Braunschweig Meteorite—A Recent L6 Chondrite Fall in Germany. *Chemie der Erde-Geochemistry* 77: 207–224.

Benkhoff, J., van Casteren, J., Hayakawa, H., Fujimoto, M., Laakso, H., Novara, M., Ferri, P., Middleton, H. R., and Ziethe, R. 2010. BepiColombo–Comprehensive

Exploration of Mercury: Mission Overview and Science Goals. *Planetary and Space Science* 58: 2–20.

Bischoff, A., and Patzek, M. 2024. Elmshorn (H3-6-an) and Ribbeck (aubrite) - Mineralogy of two recent meteorite falls in Germany (abstract #6144). 86th Annual Meeting of the Meteoritical Society. LPI Contribution No. 3036.

Bischoff, A., and Stöffler, D. 1992. Shock Metamorphism as a Fundamental Process in the Evolution of Planetary Bodies: Information from Meteorites. *European Journal of Mineralogy* 4: 707–755.

Bischoff, A., and Schultz, L. 2004. Abundance and Meaning of Regolith Breccias among Meteorites. *Meteoritics & Planetary Science* 39: A15.

Bischoff, A., Rubin, A. E., Keil, K., and Stöffler, D. 1983. Lithification of Gas-Rich Chondrite Regolith Breccias by Grain Boundary and Localized Shock Melting. *Earth and Planetary Science Letters* 66: 1–10.

Bischoff, A., Scott, E. R. D., Metzler, K., and Goodrich, C. A. 2006. Nature and Origins of Meteoritic Breccias. In *Book Chapter in "Meteorites and the Early Solar System II"*, edited by D. S. Lauretta, and H. Y. McSween, Jr., 679–712. Tucson, AZ: University of Arizona.

Bischoff, A., Horstmann, M., Pack, A., Laubenstein, M., and Haberer, S. 2010. Asteroid 2008 TC$_3$—Almahata Sitta: A Spectacular Breccia Containing Many Different Ureilitic and Chondritic Lithologies. *Meteoritics & Planetary Science* 45: 1638–56.

Bischoff, A., Barrat, J.-A., Bauer, K., Burkhardt, C., Busemann, H., Ebert, S., Gonsior, M., et al. 2017. The Stubenberg Meteorite—An LL6 Chondrite Fragmental Breccia Recovered Soon after Precise Prediction of the Strewn Field. *Meteoritics & Planetary Science* 52: 1683–1703.

Bischoff, A., Schleiting, M., Wieler, R., and Patzek, M. 2018. Brecciation among 2280 Ordinary Chondrites—Constraints on the Evolution of their Parent Bodies. *Geochimica et Cosmochimica Acta* 238: 516–541.

Bischoff, A., Barrat, J.-A., Berndt, J., Borovicka, J., Burkhardt, C., Busemann, H., Hakenmüller, J., et al. 2019. The Renchen L5-6 Chondrite Breccia—The First Confirmed Meteorite Fall from Baden-Württemberg (Germany). *Geochemistry—Chemie der Erde* 79: 125525.

Bischoff, A., Schleiting, M., and Patzek, M. 2019. Shock Stage Distribution of 2280 Ordinary Chondrites—Can Bulk Chondrites with a Shock Stage S6 Exist as Individual Rocks? *Meteoritics & Planetary Science* 54: 2189–2202.

Bischoff, A., Alexander, C. M. O'D., Barrat, J.-A., Burkhardt, C., Busemann, H., Degering, D., Di Rocco, T., et al. 2021. The Old, Unique C1 Chondrite Flensburg—Insight into the First Processes of Aqueous Alteration, Brecciation, and the Diversity of Water-Bearing Parent Bodies and Lithologies. *Geochimica et Cosmochimica Acta* 293: 142–186.

Bischoff, A., Bannemann, L., Decker, S., Ebert, S., Haberer, S., Heitmann, U., Horstmann, M., et al. 2022. Asteroid 2008 TC$_3$, Not a Polymict Ureilitic but a Polymict C1 Chondrite Parent Body? Survey of 249 Almahata Sitta Fragments. *Meteoritics & Planetary Science* 57: 1339–64.

Bischoff, A., Patzek, M., Peters, S. T. M., Barrat, J.-A., Di Rocco, T., Pack, A., Ebert, S., Jansen, C. A., and Kmieciak, K. 2022. The Chondrite Breccia of Antonin (L4-5)—A New Meteorite Fall from Poland with a Heterogeneous Distribution of Metal. *Meteoritics & Planetary Science* 57: 2127–42.

Bischoff, A., Patzek, M., Alosius, R. M. L., Barrat, J.-. A., Berndt, J., Busemann, H., Degering, D., et al. 2024. The Anomalous Polymict Ordinary Chondrite Breccia of Elmshorn (H3-6)—Late re-Accretion after Collision between Two Ordinary Chondrite Parent Bodies, Complete Disruption, and Mixing Possibly about 2.8 Gyr Ago. *Meteoritics & Planetary Science* (accepted). https://doi.org/10.1111/maps.14193.

Brunetto, R., and Strazzulla, G. 2005. Elastic Collisions in Ion Irradiation Experiments: A Mechanism for Space Weathering of Silicates. *Icarus* 179: 265–273.

Brunetto, R., Lantz, C., Ledu, D., Baklouti, D., Barucci, M. A., Beck, P., Delauche, L., et al. 2014. Ion Irradiation of Allende Meteorite Probed by Visible, IR, and Raman Spectroscopies. *Icarus* 237: 278–292.

Bunch, T. E., and Fuchs, L. H. 1969. A New Mineral: Brezinaite, Cr3S4, and the Tucson Meteorite. *American Mineralogist: Journal of Earth and Planetary Materials* 54: 1509–18.

Burbine, T. H., McCoy, T. J., Meibom, A., Gladman, B., and Keil, K. 2002. Meteoritic Parent Bodies: Their Number and Identification. In *Asteroids III*, edited by W. F. Bottke, Jr., A. Cellino, P. Paolicchi, and R. P. Binzel, 653–667. Tucson, AZ: University of Arizona.

Busemann, H., and Eugster, O. 2002. The Trapped Noble Gas Component in Achondrites. *Meteoritics & Planetary Science* 37: 1865–91.

Casanova, I., Keil, K., and Newsom, H. 1993. Composition of Metal in Aubrites: Constraints on Core Formation. *Geochimica et Cosmochimica Acta* 57: 675–682.

Cantillo, D. C., Ridenhour, K. I., Battle, A., Joyce, T., Nunez, B. J., Pearson, N., and Reddy, V. 2024. Laboratory Spectral Characterization of Ribbeck Aubrite: Meteorite Sample of Earthi Mpacting near-Earth Asteroid 2024 BX1. *The Planetary Science Journal* 5: 138 14 pp.

Clay, P. L., O'Driscoll, B., Upton, B. G. J., and Busemann, H. 2014. Characteristics of Djerfisherite from Fluid-Rich, Metasomatized Alkaline Intrusive Environments and Anhydrous Enstatichondrites and Achondrites. *American Mineralogist* 99: 1683–93.

Ćuk, M., Gladman, B. J., and Nesvorný, D. 2014. Hungaria Asteroid Family as the Source of Aubrite Meteorites. *Icarus* 239: 154–59.

Dalcher, N., Caffee, M. W., Nishiizumi, K., Welten, K. C., Vogel, N., Wieler, R., and Leya, I. 2013. Calibration of Cosmogenic Noble Gas Production in Ordinary Chondrites Based on ^{36}Cl-^{36}Ar Ages. Part 1: Refined Produced Rates for Cosmogenic ^{21}Ne and ^{38}Ar. *Meteoritics & Planetary Science* 48: 1841–62.

DDEP. 2023. DDEP (Decay Data Evaluation Project) website. http://www.nucleide.org/Laraweb/index.php.

Drummond, J. D. 1981. A Test of Comet and Meteor Shower Associations. *Icarus* 45: 545–553.

Eberhardt, P., Geiss, J., and Lutz, H. 1963. Neutrons in Meteorites. In *Earth Science and Meteoritics*, 143–168. Amsterdam: North-Holland.

Ebert, S., and Bischoff, A. 2016. The Stubenberg (Bavaria) Ordinary Chondrite Breccia: The Latest German Meteorite Fall. *Meteoritics & Planetary Science* 51: 6137.

Eugster, O., Herzog, G. F., Marti, K., and Caffee, M. W. 2006. Irradiation Records, Cosmic-Ray Exposure Ages, and Transfer Times of Meteorites. In *Meteorites and the Early Solar System II*, edited by D. S. Lauretta, and H. Y. McSween, Jr., 829–851. Tucson, AZ: University of Arizona.

Farnocchia, D. 2024. JPL Small-Body Database Lookup. https://ssd.jpl.nasa.gov/tools/sbdb_lookup.html#/?sstr=2024%20BX1&view=OPC.

Fogel, R. A. 1997. A New Aubrite Basalt Vitrophyre from the LEW 87007 Aubrite. *28th Lunar and Planetary Science Conference*, pp. 369–70.

Fuchs, L. H. 1966. Djerfisherite, Alkali Copper-Iron Sulfide, a New Mineral from the Kota-Kota and St. Mark's Enstatite Chondrites. *Science* 153: 166–67.

Gaffey, M. J., Reed, K. L., and Kelley, M. S. 1992. Relationship of E-Type Apollo Asteroid 3103 (1982 BB) to the Enstatite Achondrite Meteorites and the Hungaria Asteroids. *Icarus* 100: 95–109.

Galiazzo, M., Bazso, A., and Dvorak, R. 2013. Fugitives from the Hungaria Region: Close Encounters and Impacts with Terrestrial Planets. *Planetary and Space Science* 84: 5–13.

Garrison, D. H., Rao, M. N., and Bogard, D. D. 1995. Solar-Proton-Produced Neon in Shergottite Meteorites and Implications for their Origin. *Meteoritics* 30: 738–747.

Gladman, B., and Coffey, J. 2009. Mercurian Impact Ejecta: Meteorites and Mantle. *Meteoritics & Planetary Science* 44: 285–291.

Gritsevich, M., Vinnikov, V., Kohout, T., Tóth, J., Peltoniemi, J., Turchak, L., and Virtanen, J. 2014. A Comprehensive Study of Distribution Laws for the Fragments of Košice Meteorite. *Meteoritics & Planetary Science* 49: 328–345.

Grott, M., Knollenberg, J., Hamm, M., Ogawa, K., Jaumann, R., Otto, K. A., Delbo, M., et al. 2019. Low Thermal Conductivity Boulder with High Porosity Identified on C-Type Asteroid (162173) Ryugu. *Nature Astronomy* 3: 971–76.

Haack, H., Sørensen, A. N., Bischoff, A., Patzek, M., Barrat, J.-A., Midtskoge, S., Stempel, E., et al. 2019. Ejby—A New H5/6 Ordinary Chondrite Fall in Copenhagen, Denmark. *Meteoritics & Planetary Science* 54: 1853–69.

Hamann, C., Greshake, A., Hecht, L., Jenniskens, P., Kaufmann, F., Luther, R., Van den Neucker, A., et al. 2024. Initial Analysis of the Ribbeck Aubrite Recovered from Asteroid 2024 BX1 (abstract #6418). 86th Annual Meeting of the Meteoritical Society. LPI Contribution No. 3036.

Helbert, J., Moroz, L. V., Maturilli, A., Bischoff, A., Warell, J., Sprague, A., and Palomba, E. 2007. A Set of Laboratory Analogue Materials for the MERTIS Instrument on the ESA BepiColombo Mission to Mercury. *Advances in Space Research* 40: 272–79.

Herwartz, D., Pack, A., Friedrichs, B., and Bischoff, A. 2014. Identification of the Giant Impactor Theia in Lunar Rocks. *Science* 344: 1146–50.

Hicks, M., Lawrence, K., Chesley, S., Chesley, J., Rhoades, H., Elberhar, S., Carcione, A., and Borlase, R. 2013. Palomar Spectroscopy of Near-Earth Asteroids 137199 (1999 KX4), 152756 (1999 JV3), 163249 (2002 GT), 163364 (2002 OD20), and 285263 (1998 QE2). The Astronomer's Telegram #5132. https://www.astronomerstelegram.org/?read=5132.

Hidaka, H., Ebihara, M., and Yoneda, S. 1999. High Fluences of Neutrons Determined from Sm and Gd Isotopic Compositions in Aubrites. *Earth and Planetary Science Letters* 173: 41–51.

Hiesinger, H., Helbert, J., and Mertis Co-I Team. 2010. The Mercury Radiometer and Thermal Infrared Spectrometer (MERTIS) for the BepiColombo Mission. *Planetary and Space Science* 58: 144–165.

Hiesinger, H., Helbert, J., Alemanno, G., Bauch, K. E., D'Amore, M., Maturilli, A., Morlok, A., Reitze, M. P., Stangarone, C., and Stojic, A. N. 2020. Studying the Composition and Mineralogy of the Hermean Surface with the Mercury Radiometer and Thermal Infrared Spectrometer (MERTIS) for the BepiColombo Mission: An Update. *Space Science Reviews* 216: 110.

Hohenberg, C. M., Marti, K., Podosek, F. A., Reedy, R. C., and Shirck, J. R. 1978. Comparisons between Observed and Predicted Cosmogenic Noble Gases in Lunar Samples. *Proceedings of the 9th Lunar and Planetary Science Conference*, pp. 2311–44.

Horstmann, M., and Bischoff, A. 2014. The Almahata Sitta Polymict Breccia and the Late Accretion of Asteroid 2008 TC₃—Invited Review. *Chemie der Erde—Geochemistry* 74: 149–184.

Irving, A. J., Kuehner, S. M., Bunch, T. E., Ziegler, K., Chen, G., Herd, C. D. K., Conrey, R. M., and Ralew, S. 2013. Ungrouped Mafic Achondrite Northwest Africa 7325: A Reduced, Iron-Poor Cumulate Olivine Gabbro from a Differentiated Planetary Parent Body. *44th Lunar and Planetary Science Conference*, abstract #2164.

Jenniskens, P., Fries, M. D., Yin, Q.-Z., Zolensky, M., Krot, A. N., Sandford, S. A., Sears, D., et al. 2012. Radar-Enabled Recovery of the Sutter's Mill Meteorite, a Carbonaceous Chondrite Regolith Breccia. *Science* 338: 1583–87.

Jet Propulsion Laboratory. 2024. JPL Small-Body Database Lookup. https://ssd.jpl.nasa.gov/tools/sbdb_lookup.html#/?sstr=2024%20BE1&view=OPC.

Keil, K. 1982. Composition and Origin of Chondritic Breccias. In *Workshop on Lunar Breccias and Soils and their Meteoritic Analogs*, edited by G. J. Taylor, and L. L. Wilkening, 65–83. LPI Technical Report 82-02. Houston, TX: Lunar and Planetary Institute.

Keil, K. 1989. Enstatite Meteorites and their Parent Bodies. *Meteoritics* 24: 195–208.

Keil, K. 2007. Occurrence and Origin of Keilite, (Fe>0.5, Mg<0.5)S, in Enstatite Chondrite Impact-Melt Rocks and Impact-Melt Breccias. *Chemie der Erde–Geochemistry* 67: 37–54.

Keil, K. 2010. Enstatite Achondrite Meteorites (Aubrites) and the Histories of their Asteroidal Parent Bodies. *Chemie der Erde* 70: 295–317.

Keil, K., and Brett, R. 1974. Heideite, $(Fe,Cr)_{1+x}$ $(Ti,Fe)_2S_4$, a New Mineral in the Bustee Enstatite Achondrite. *American Mineralogist: Journal of Earth and Planetary Materials* 59: 465–470.

Keil, K., and Fredriksson, K. 1963. Electron Microprobe Analysis of some Rare Minerals from the Norton County Achondrite. *Geochimica et Cosmochimica Acta* 27: 939–947.

Keil, K., Ntaflos, T., Taylor, G. J., Brearley, A. J., Newson, H. E., and Romig, A. D. 1989. The Shallowater Aubrite: Evidence for Origin by Planetesimal Impact. *Geochimica et Cosmochimica Acta* 53: 3291–3307.

Keil, K., Haack, H., and Scott, E. R. D. 1994. Catastrophic Fragmentation of Asteroids: Evidence from Meteorites. *Planetary and Space Science* 42: 1109–22.

Keil, K., Stöffler, D., Love, S. G., and Scott, E. R. D. 1997. Constraints on the Role of Impact Heating and Melting in Asteroids. *Meteoritics & Planetary Science* 32: 349–363.

Keller, L. P., and McKay, D. S. 1997. The Nature and Origin of Rims on Lunar Soil Grains. *Geochimica et Cosmochimica Acta* 61: 2331–41.

Keller, L. P., and McKay, D. S. 1993. Discovery of Vapor Deposits in the Lunar Regolith. *Science* 261: 1305–7.

Kieffer, S. W. 1975. From Regolith to Rock by Shock. *The Moon* 13: 301–320.

Kroll, H. 1973. Estimation of the Al,Si Distribution of Feldspars from the Lattice Translations Tr[110] and Tr[1$\bar{1}$0]. *Contributions to Mineralogy and Petrology* 39: 141–156.

Krot, A. N., Keil, K., Goodrich, C. A., and Scott, E. R. D. 2004. Classification of Meteorites. *Treatise on Geochemistry, Meteorites, Comets and Planets* 1: 83–128.

Lentfort, S., Bischoff, A., Ebert, S., and Patzek, M. 2021. Classification of CM Chondrite Breccias—Implications for the Evaluation of Samples from the OSIRIS-REx and Hayabusa2 Missions. *Meteoritics & Planetary Science* 56: 127–147.

Leya, I., and Masarik, J. 2009. Cosmogenic Nuclides in Stony Meteorites Revisited. *Meteoritics & Planetary Science* 44: 1061–86.

Leya, I., Hirtz, J., and David, J.-C. 2021. Galactic Cosmic Rays, Cosmic-Ray Variations, and Cosmogenic Nuclides in Meteorites. *The Astrophysical Journal* 910: 136.

Li, M., Huang, Y., and Gong, S. 2019. Assessing the Risk of Potentially Hazardous Asteroids Through Mean Motion Resonances Analyses. *Astrophysics and Space Science* 364: 78.

Lipschutz, M. E., Verkouteren, R. M., Sears, D. W. G., Hasan, F., Prinz, M., Weisberg, M. K., Nehru, C. E., Delaney, J. S., Grossman, L., and Boily, M. 1988. Cumberland Falls Chondritic Inclusions: III. Consortium Study of Relationship to Inclusions in Allan Hills 78113 Aubrite. *Geochimica et Cosmochimica Acta* 52: 1835–48.

Lodders, K., and Fegley, B., Jr. 1998. *The Planetary Scientist's Companion*. New York: Oxford University Press. 371.

Loeffler, M. J., Dukes, C. A., Christoffersen, R., and Baragiola, R. A. 2016. Space Weathering of Silicates Simulated by Successive Laser Irradiation: In Situ Reflectance Measurements of Fo90, Fo99+, and SiO_2. *Meteoritics & Planetary Science* 51: 261–275.

Lonsdale, J. T. 1947. The Pena Blanca Spring Meteorite, Brewster County, Texas. *American Mineralogist* 32: 354–364.

Lorenz, C. A., Ivanova, M. A., Kurat, G., and Brandstaetter, F. 2005. FeO-Rich Xenoliths in the Staroye Pesyanoe Aubrite. *36th Lunar and Planetary Science Conference*, abstract #1612.

Lorenzetti, S., Eugster, O., Busemann, H., Marti, K., Burbine, T. H., and McCoy, T. 2003. History and Origin of Aubrites. *Geochimica et Cosmochimica Acta* 67: 557–571.

Love, S. G., and Keil, K. 1995. Recognizing Mercurian meteorites. *Meteoritics* 30: 269–278.

Love, J. J., Hill, D. H., Domanik, K. J., Lauretta, D. S., Drake, M. J., and Killgore, M. 2005. NWA 2736: An Unusual New Graphite-Bearing Aubrite. *36th Lunar and Planetary Science Conference*, abstract #1913.

Macke, R. J., Britt, D. T., and Consolmagno, G. J. 2011. Density, Porosity, and Magnetic Susceptibility of Achondritic Meteorites. *Meteoritics & Planetary Science* 46: 311–326.

Markus, K., Arnold, G., Moroz, L., Henckel, D., and Hiesinger, H. 2024. Laboratory Reflectance Spectra of Enstatite and Oldhamite Mixtures for Comparison with Earth-Based Reflectance Spectra of Asteroid 2867 Šteins

and Mercury. *Planetary and Space Science* 244: 105887. https://doi.org/10.1016/j.pss.2024.105887.

Marshal, R. M., Patzek, M., and Rüsch, O. 2024. Characterization of the Micrometer Scale Surface Roughness of Meteoritic Samples. *Icarus* 412: 115984.

Marti, K., and Graf, T. 1992. Cosmic-Ray Exposure History of Ordinary Chondrites. *Annual Review of Earth and Planetary Sciences* 20: 221–243.

Marti, K., Eberhardt, P., and Geiss, J. 1966. Spallation, Fission, and Neutron Capture Anomalies in Meteoritic Krypton and Xenon. *Zeitschrift für Naturforschung* 21a: 398–413.

Martschini, M., Lachner, J., Hain, K., Kern, M., Marchhart, O., Pitters, J., Priller, A., et al. 2022. 5 Years of Ion-Laser Interaction Mass Spectrometry—Status and Prospects of Isobar Suppression in AMS by Lasers. *Radiocarbon* 64: 555–568.

McCoy, T. J., Rosenshein, E. B., and Dickinson, T. I. 1999. A Unique Oxide-Bearing Clast in the Aubrite Allan Hills 84008: Evidence for Oxidation during Magmatic Processes. *30th Lunar and Planetary Science Conference*, abstract #1347.

McCoy, T. J., Dickinson, T. L., and Burbine, T. H. 2000. Rare Earth Elements in Coexisting Sulfides in the Allan Hills 84008 Aubrite: Clues to Aubrite Genesis. *Meteoritics & Planetary Science* 35: A105–A106.

Mernagh, T. P. 1991. Use of the Laser Raman Microprobe for Discrimination amongst Feldspar Minerals. *Journal of Raman Spectroscopy* 22: 453–57.

Minor Planet Center. 2024a. Minor Planet Electronic Circular (MPEC) 2024-B76, 2024 January 21. https://www.minorplanetcenter.net/mpec/K24/K24B76.html.

Minor Planet Center. 2024b. Minor Planet Electronic Circular (MPEC) 2024-E02, 2024 March 1. https://www.minorplanetcenter.net/mpec/K24/K24E02.html.

Minor Planet Center. 2024c. MPCOrb Database. https://www.minorplanetcenter.net/data.

Minor Planet Center. 2024d. Minor Planet Electronic Circular (MPEC) 2024-B53. https://www.minorplanetcenter.net/mpec/K24/K24B53.html.

Mittlefehldt, D. W. 2004. Achondrites. In *Treatise on Geochemistry, Vol. 1: Meteorites, Comets, and Planets*, edited by A. M. Davis, 291–324. Oxford: Elsevier.

Mittlefehldt, D. W., McCoy, T. J., Goodrich, C. A., and Kracher, A. 1998. Non-Chondritic Meteorites from Asteroidal Bodies. In *Planetary Materials*, edited by J. J. Papike, 4-1-4-495. *Reviews in Mineralogy*, Vol. 36. Mineralogical Society of America.

Molaro, J. L., Walsh, K. J., Jawin, E. R., Ballouz, R. L., Bennett, C. A., DellaGiustina, D. N., Golish, D. R., et al. 2020. In Situ Evidence of Thermally Induced Rock Breakdown Widespread on Bennu's Surface. *Nature Communications* 11: 2913.

Morlok, M., Weber, I., Stojic, A. N., Sohn, M., Bischoff, A., Martin, D., Hiesinger, H., and Helbert, J. 2020. Mid-Infrared Reflectance Spectroscopy of Aubrite Components. *Meteoritics & Planetary Science* 55: 2080–96.

Namur, O., and Charlier, B. 2016. Silicate Mineralogy at the Surface of Mercury. *Nature Geoscience* 10: 9–13.

Nicodemus, F. E. 1965. Directional Reflectance and Emissivity of an Opaque Surface. *Applied Optics* 4: 767–775.

Niese, S., Köhler, M., and Gleisberg, B. 1998. Low-Level Counting Techniques in the Underground Laboratory "Felsenkeller" in Dresden. *Journal of Radioanalytical and Nuclear Chemistry* 233: 167–172.

Norris, T. L., Gancarz, A. J., Rokop, D. J., and Thomas, K. W. 1983. Half-Life of ^{26}Al. *Journal of Geophysical Research* 8: B331–B333.

Okada, A., and Keil, K. 1982. Caswellsilverite, NaCrSr: A New Mineral in the Norton County Enstatite Achondrite. *American Mineralogist* 67: 132–36.

Okada, A., Keil, K., Leonard, B. F., and Hutcheon, I. D. 1985. Schöllhornite, $Na_{0.3}(H_2O)[CrS_2]$, a New Mineral in the Norton County Enstatite Achondrite. *American Mineralogist* 70: 638–643.

Okada, A., Keil, K., Taylor, G. J., and Newsom, H. 1988. Igneous History of the Aubrite Parent Asteroid: Evidence from the Norton County Enstatite Achondrite. *Meteoritics* 23: 59–74.

Pack, A., and Herwartz, D. 2014. The Triple Oxygen Isotope Composition of the Earth Mantle and Understanding $\Delta^{17}O$ Variations in Terrestrial Rocks and Minerals. *Earth and Planetary Science Letters* 390: 138–145.

Pack, A., Tanaka, R., Hering, M., Sengupta, S., Peters, S., and Nakamura, E. 2016. The Oxygen Isotope Composition of San Carlos Olivine on VSMOW2-SLAP2 Scale. *Rapid Communications in Mass Spectrometry* 30: 1495–1504.

Pack, A., Höweling, A., Hezel, D. C., Stefanak, M., Beck, A. K., Peters, S. T. M., Sengupta, S., Herwartz, D., and Folco, L. 2017. Tracing the Oxygen Isotope Composition of the Upper Earth Atmosphere Using Cosmic Spherules. *Nature Communications* 8: 15702.

Patzek, M., and Rüsch, O. 2022. Experimentally Induced Thermal Fatigue on Lunar and Eucrite Meteorites— Influence of the Mineralogy on Rock Breakdown. *Journal of Geophysical Research: Planets* 127: e2022JE007306.

Patzek, M., Rüsch, O., and Molaro, J. L. 2024. On the Response of Chondrites to Diurnal Temperature Change —Experimental Simulation of Asteroidal Surface Conditions. *Journal of Geophysical Research: Planets* 129: e2023JE007944.

Peters, S. T. M., Alibabaie, N., Pack, A., McKibbin, S. J., Raeisi, D., Nayebi, N., Torab, F., Ireland, T., and Lehmann, B. 2020. Triple Oxygen Isotope Variations in Magnetite from Iron-Oxide Deposits, Central Iran, Record Magmatic Fluid Interaction with Evaporite and Carbonate Host Rocks. *Geology* 48: 211–15.

Peters, S. T. M., Fischer, M. B., Pack, A., Szilas, K., Appel, P. W. U., Muenker, C., Dallai, L., and Marien, C. S. 2021. Tight Bounds on Missing Late Veneer in Early Archean Peridotite from Triple Oxygen Isotopes. *Geochemical Perspectives Letters* 18: 27–31.

Pieters, C. M., and Noble, S. K. 2016. Space Weathering on Airless Bodies. *Journal of Geophysical Research, Planets* 121: 1865–84.

Poupeau, G., Kirsten, T., Steinbrunn, F., and Storzer, D. 1974. The Records of Solar Wind and Solar Flares in Aubrites. *Earth and Planetary Science Letters* 24: 229–241.

Reitze, M. P., Weber, I., Kroll, H., Morlok, A., Hiesinger, H., and Helbert, J. 2020. Mid-Infrared Spectroscopy of Alkali Feldspar Samples for Space Application. *Mineralogy and Petrology* 114: 453–463.

Reitze, M. P., Weber, I., Morlok, A., Hiesinger, H., Bauch, K. E., Stojic, A. N., and Helbert, J. 2021. Mid-Infrared Spectroscopy of Crystalline Plagioclase Feldspar Samples with Various Al,Si Order and Implications for Remote Sensing of Mercury and Other Terrestrial Solar System Objects. *Earth and Planetary Science Letters* 554: 116697.

Reitze, M. P., Renggli, C. J., Morlok, A., Weber, I., Hiesinger, H., Stojic, A. N., Pasckert, J. H., Bauch, K. E., Schmedemann, N., and Helbert, J. 2024. Infrared Spectra of the Solid Solution between Oldhamite and Niningerite (CaS-MgS): A Complex Case in the Laboratory. *55th Lunar Planetary Science Conference*, abstract #1858.

Rendtel, Molau, S., Möller, A., Sachs, O., Lenzen, O., and Hankey, M. 2024. Ribbeck Meteorite – 2024 BX1 and the Fall of an Aubrite in Ribbeck on 2024 January 21. *WGN, The Journal of the IMO* 52: 29–39.

Renggli, C. J., Klemme, S., Morlok, A., Berndt, J., Weber, I., Hiesinger, H., and King, P. L. 2022. Sulfides and Hollows Formed on Mercury's Surface by Reactions with Reducing S-Rich Gases. *Earth and Planetary Science Letters* 593: 117647.

Riebe, M. E. I., Welten, K. C., Meier, M. M. M., Wieler, R., Barth, M. I. F., Ward, D., Laubenstein, M., et al. 2017. Cosmic-Ray Exposure Ages of Six Chondritic Almahata Sitta Fragments. *Meteoritics & Planetary Science* 52: 2353–74.

Rochette, P., Gattacceca, J., Bourot-Denise, M., Consolmagno, G. J., Folco, L., Kohout, T., Pesonen, L., and Sagnotti, L. 2009. Magnetic Classification of Stony Meteorites: 3. Achondrites. *Meteoritics & Planetary Science* 44: 405–428.

Rubin, A. E., and Turrin, B. D. 2023. Nature and Timing of a Significant Reduction Event on the L-Chondrite Parent Asteroid. *Meteoritics & Planetary Science* 59: 836–857. https://doi.org/10.1111/maps.14088.

Rubin, A. E., Keil, K., Taylor, G. J., Ma, M. S., Schmitt, R. A., and Bogard, D. D. 1981. Derivation of a Heterogeneous Lithic Fragment in the Bovedy L-Group Chondrite from Impact-Melted Porphyritic Chondrules. *Geochimica et Cosmochimica Acta* 45: 2213–28.

Rubin, A. E., Rehfeldt, A., Peterson, E., Keil, K., and Jarosewich, E. 1983. Fragmental Breccias and the Collisional Evolution of Ordinary Chondrite Parent Bodies. *Meteoritics* 18: 179–196.

Rubin, A. E., Scott, E. R. D., Taylor, G. J., Keil, K., Allen, J. S. B., Mayeda, T. K., Clayton, R. N., and Bogard, D. D. 1983. Nature of the H Chondrite Parent Body Regolith: Evidence from the Dimmitt Breccia. *13th Lunar and Planetary Science Conference*, A741–54.

Rubin, A. E., Scott, E. R. D., and Keil, K. 1997. Shock Metamorphism of Enstatite Chondrites. *Geochimica et Cosmochimica Acta* 61: 847–858.

Rüfenacht, M., Morino, P., Lai, Y.-J., Fehr, M. A., Haba, M. K., and Schönbächler, M. 2023. Genetic Relationships of Solar System Bodies Based on their Nucleosynthetic Ti Isotope Compositions and Sub-Structures of the Solar Protoplanetary Disk. *Geochimica et Cosmochimica Acta* 355: 110–125.

Schönbächler, M., Rehkämper, M., Lee, D.-C., and Halliday, A. N. 2004. Ion Exchange Chromatography and High Precision Isotopic Measurements of Zirconium by MC-ICP-MS. *Analyst* 129: 32–37.

Shaddad, M. H., Jenniskens, P., Numan, D., Kudoda, A. M., Elsir, S., Riyad, I. F., Ali, A. E., et al. 2010. The Recovery of Asteroid 2008 TC3. *Meteoritics & Planetary Science* 45: 1557–89.

Shrbeny, L., Krzesinska, A. M., Borovicka, J., Spurný, P., Tyminski, Z., and Kmieciak, K. 2022. Analysis of the Daylight Fireball of July 15, 2021, Leading to Meteorite Fall and Find near Antonin, Poland, and a Description of

the Recovered Meteorite. *Meteoritics & Planetary Science* 57: 2108–26.

Sprague, A., Deutsch, L. K., Hora, J., Fazio, G. G., Ludwig, B., Emery, J., and Hoffmann, W. F. 2000. Mid-Infrared (8.1–12.5 μm) Imaging of Mercury. *Icarus* 147: 421–432.

Spurný, P. 2016. Instrumentally Documented Meteorite Falls: Two Recent Cases and Statistics from all Falls. In *Asteroids: New Observations, New Models. Proceedings IAU Symposium* 318, edited by S. Chesley, A. Morbidelli, R. Jedicke, and D. Farnocchia, 69–79. Cambridge: Cambridge University Press.

Spurný, P., Borovicka, J., Haloda, J., Shrbeny, L., and Heinlein, D. 2016. Two Very Precisely Instrumentally Documented Meteorite Falls: Žďár Nad Sázavou and Stubenberg—Prediction and Reality. *Meteoritics & Planetary Science* 51 Special Issue: A591.

Spurný, P., Borovička, J., Baumgarten, G., Haack, H., Heinlein, D., and Sørensen, A. N. 2017. Atmospheric Trajectory and Heliocentric Orbit of the Ejby Meteorite Fall in Denmark on February 6, 2016. *Planetary and Space Science* 143: 192–98.

Spurný, P., Borovička, J., Shrbený, L., Hankey, M. R., and Neubert, R. 2024. Atmospheric Entry and Fragmentation of Small Asteroid 2024 BX1: Bolide Trajectory, Orbit, Dynamics, Light Curve, and Spectrum. *Astronomy and Astrophysics* 686: A67. https://arxiv.org/pdf/2403.00634.pdf.

Steenstra, E., and van Westrenen, W. 2020. Geochemical Constraints on Core-Mantle Differentiation in Mercury and the Aubrite Parent Body. *Icarus* 340: 113621.

Stöffler, D., Bischoff, A., Buchwald, V., and Rubin, A. E. 1988. Shock Effects in Meteorites. In *Meteorites and the Early Solar System*, edited by J. F. Kerridge, and M. S. Matthews, 165–202. Tucson, AZ: The University of Arizona Press.

Stöffler, D., Keil, D., and Scott, E. R. D. 1991. Shock Metamorphism of Ordinary Chondrites. *Geochimica et Cosmochimica Acta* 55: 3845–67.

Stöffler, D., Hamann, C., and Metzler, K. 2018. Shock Metamorphism of Planetary Silicate Rocks and Sediments: Proposal for an Updated Classification System. *Meteoritics & Planetary Science* 53: 5–49.

Stojic, A. N., Weber, I., Morlok, A., Pavlov, S. G., Hiesinger, H., Reitze, M. P., Maturilli, A., et al. 2023. Simulation of Surface Regolith Gardening and Impact Associated Melt Layer Production under Ns-Pulsed Laser Ablation. *Icarus* 391: 115344.

Sun, L., and Lucey, P. G. 2023. Searching for Mantle Dunite Candidates around the Imbrium Basin among the Boulder Population Using High Resolution Mineral Mapping. *Earth and Planetary Science Letters* 610: 118074.

Tatsumi, E., Sakatani, N., Riu, L., Matsuoka, M., Honda, R., Morota, T., Kameda, S., et al. 2021. Spectrally Blue Hyrated Parent Body of Asteroid (162173) Ryugu. *Nature Communications* 12: 5837.

Taylor, L. A., Pieters, C. M., Keller, L. P., Morris, R. V., and McKay, D. S. 2001. Lunar Mare Soils: Space Weathering and the Major Effects of Surface-Correlated Nanophase Fe. *Journal of Geophysical Research* 106: 27985–99.

The Meteoritical Bulletin. 2024. Meteoritical Bulletin Database. https://www.lpi.usra.edu/meteor/about.php.

Tseng, C.-H. P. 1984. Calcium-Sulfite Hemihydrate Dissolution and Crystallization (Flue Gas, Desulfurization). ProQuest Dissertations and Theses, 154.

Udry, A., Wilbur, Z. E., Rahib, R. R., McCubbin, F. M., Vander, K. K., McCoy, T. J., Ziegler, K., et al. 2019.

Reclassification of Four Aubrites as Enstatite Chondrite Impact Melts: Potential Geochemical Analogs for Mercury. *Meteoritics & Planetary Science* 54: 785–810.

Unsalan, O., Jenniskens, P., Yin, Q.-Z., Kaygisiz, E., Albers, J., Clark, D. L., Granvik, M., et al. 2019. The Sariçiçek Howardite Fall in Turkey: Source Crater of HED Meteorites on Vesta and Impact Risk of Vestoids. *Meteoritics & Planetary Science* 54: 953–1008.

Van den Neucker, A., Helbert, J., Barraud, O., D'Amore, M., Verma, N., Adeli, S., Alemanno, G., et al. 2024. The Spectral Characterization of the Ribbeck Aubrite as Mercury Analog (abstract #6412). 86th Annual Meeting of the Meteoritical Society. LPI Contribution No. 3036.

Van der Plas, L., and Tobi, A. C. 1965. A Chart for Judging the Reliability of Point Counting Results. *American Journal of Science* 263: 87–90.

Warner, B. D., Harris, A. W., Vokrouhlický, D., Nesvorný, D., and Bottke, W. F. 2009. Analysis of the Hungaria Asteroid Population. *Icarus* 204: 172–182.

Watters, T. R., and Prinz, M. 1979. Aubrites: Their Origin and Relationship to Enstatite Chondrites. *Proceedings of the 10th Lunar and Planetary Science Conference*, pp. 1073–93.

Watters, T. R., and Prinz, M. 1980. Mt. Egerton and the Aubrite Parent Body. *11th Lunar and Planetary Science Conference*, pp. 1225–7.

Weber, I., Morlok, A., Bischoff, A., Hiesinger, H., Ward, D., Joy, K. H., Crowther, S. A., et al. 2016. Cosmochemical and Spectroscopic Properties of Northwest Africa 7325—A Consortium Study. *Meteoritics & Planetary Science* 51: 3–30.

Weber, I., Böttger, U., Pavlov, S. G., Hübers, H.-W., Hiesinger, H., and Jessberger, E. K. 2017. Laser Alteration on Iron Sulfides under Various Environmental Conditions. *Journal of Raman Spectroscopy* 48: 1509–17.

Weber, I., Reitze, M. P., Heeger, M., Adolphs, T., Morlok, A., Stojic, A. N., Hiesinger, H., Arlinghaus, H. F., and Helbert, J. 2021. The Effect of Excimer Laser Irradiation on Mid-IR Spectra of Mineral Mixtures for Remote Sensing. *Earth and Planetary Science Letters* 569: 117072.

Weber, I., Reitze, M. P., Morlok, A., Stojic, A. N., Hiesinger, H., Schmedemann, N., Bauch, K. E., Pasckert, J. H., and Helbert, J. 2023. Mid-IR Spectral Properties of Different Surfaces of Silicate Mixtures Before and After Excimer Laser Irradiation. *Icarus* 404: 115683.

Weyrauch, M., Horstmann, M., and Bischoff, A. 2018. Chemical Variations of Sulfides and Metal in Enstatite Chondrites—Introduction of a New Classification Scheme. *Meteoritics & Planetary Science* 53: 394–415.

Wieler, R., Huber, L., Busemann, H., Seiler, S., Leya, I., Maden, C., Masarik, J., et al. 2016. Noble Gases in 18 Martian Meteorites and Angrite Northwest Africa 7812—Exposure Ages, Trapped Gases, and a Re-Evaluation of the Evidence for Solar Cosmic Ray-Produced Neon in Shergottites and Other Achondrites. *Meteoritics & Planetary Science* 51: 407–428.

Wilbur, Z. E., Udry, A., McCubbin, F. M., van der Kaaden, K. E., DeFelice, C., Ziegler, K., Ross, D. K., et al. 2022. The Effects of Highly Reduced Magmatism Revealed Through Aubrites. *Meteoritics & Planetary Science* 57: 1387–1420.

Wilbur, Z. E., McCoy, T. J., Corrigan, C. M., Barnes, J. J., Brown, S. V., and Udry, A. 2024. The Formation of Volatile-Bearing Djerfisherite in Reduced Meteorites. *Meteoritics & Planetary Science*. https://doi.org/10.1111/maps.14220.

Williams, N. H. 2015. The origin of titanium isotopic anomalies within solar system material. PhD thesis, The University of Manchester.

Williams, N. H., Fehr, M. A., Parkinson, I. J., Mandl, M. B., and Schönbächler, M. 2021. Titanium Isotope Fractionation in Solar System Materials. *Chemical Geology* 568: 120009.

Wlotzka, F. 1993. A Weathering Scale for the Ordinary Chondrites. *Meteoritics* 28: 460.

Zhang, J., Dauphas, N., Davis, A. M., Leya, I., and Fedkin, A. 2012. The Proto-Earth as a Significant Source of Lunar Material. *Nature Geoscience* 5: 1–5.

Zhang, P., Tai, K., Li, Y., Zhang, J., Lantz, C., Hiroi, T., Matsuoka, M., et al. 2022. Diverse Space Weathering Effects on Asteroid Surfaces as Inferred Via Laser Irradiation of Meteorites. *Astronomy & Astrophysics* 659: A78.

Zipfel, J., Bischoff, A., Schultz, L., Spettel, B., Dreibus, G., Schönbeck, T., and Palme, H. 2010. Mineralogy, Chemistry, and Irradiation Record of Neuschwanstein (EL6) Chondrite. *Meteoritics & Planetary Science* 45: 1488–1501.

Zolensky, M. E., and Ivanov, A. 2003. The Kaidun Microbreccia Meteorite: A Harvest from the Inner and Outer Asteroid Belt. *Chemie der Erde-Geochemistry* 63: 185–246.

Zolensky, M., Herrin, J., Mikouchi, T., Ohsumi, K., Friedrich, J., Steele, A., Rumble, D., et al. 2010. Mineralogy and Petrography of the Almahata Sitta Ureilite. *Meteoritics & Planetary Science* 45: 1618–37.

SUPPORTING INFORMATION

Additional supporting information may be found in the online version of this article.

Data S1. The poem of Theodor Fontane "Herr von Ribbeck zu Ribbeck im Havelland in German and English".

Data S2. The analytical methods in detail.

Table S1. The list of the recovered Ribbeck specimen registered by our group.

Figure S1. Images of some studied samples.

Figure S2. Images of complete meteorite specimens.

Figure S3. Images of samples by computed tomography.

Figure S4. Raman Spectra from unusual, "altered" phases.

Figure S5. Magnetic susceptibility of Ribbeck and other aubrites

Figure S6. ^{26}Al from gamma and instrumental accelerator mass spectrometry.

Figure S7. Specific ^{22}Na activity measured by gamma spectrometry and related shielding depth.